Fraunhofer IOF

Quantum sensing with undetected light for Earth observation - ULEO

Final Report (FR)

Doc.-No.:	FR-IOF-01
Issue:	03
Date:	30.10.2025

Author:	Marta Gilaberte Basset Carlos Melo Luna Valerio Flavio Gili	date/ signature	Marta Gilaberte Basset Digitally signed by Marta Gilaberte Basset Date: 2025.10.30 10:58:45 +01'00'

1 CHANGE RECORD

Issue	Date	Authorization	Description of Change	Pages
01	15.08.2025		ULEO final report initial document	
02	18.09.2025		Implementation of actions defined during the ULEO final review – co-location meeting (04.09.2025)	
03	30.10.2025		Implementation of actions defined during ULEO close out meeting (23.09.2025)	

Contents

2 INTRODUCTION

The aim of ULEO project is to assess the quantum advantage and feasibility of quantum sensing techniques in Earth observation scenarios. This initial study is based on the results from both, an experimental analysis of the atmospheric effects on the detected image quality for an interferometric scheme in low gain, as well as a detailed simulation analysis of photon flux losses in a real Earth observation scenario.

The primary driving force for conducting this study is the substantial potential of quantum imaging and spectroscopy, especially through Quantum Imaging with Undetected Light (QIUL) techniques, to reduce the payload requirements of infrared (IR) and ultraviolet (UV) sensors onboard the satellites. This includes reductions in volume, weight, power consumption, and critical operational components, like cryostats for IR detection.

QIUL operates on a nonlinear interferometric principle. Within the interferometer, a nonlinear crystal (NLC) is pumped by a laser to generate down-converted light via spontaneous parametric down-conversion (SPDC). The SPDC process produces correlated photon pairs (signal and idler) that are correlated in various degrees of freedom, such as frequency, momentum, and position. This quantum light source can be engineered such that the signal and idler beams exhibit different wavelengths (non-degenerate SPDC); for instance, one beam may be in the IR range while the other is in the visible range. The signal and idler beams are directed through different arms of the interferometer, with one beam (e.g., the IR light) interacting with the sample while the other beam (e.g., the visible light) is used to capture the image of the object on the camera.

Due to induced coherence between the signal and idler beams, any alteration in the interference pattern caused by the presence of an object in the IR beam will be detected by the camera through the interference with the visible beam. The spatial correlations enable the mapping of a point on the object to a point on the camera, thus generating the image of the object. This image conveys not only spatial information of the object but also its transmission and induced phase relative to the illumination wavelength. The strength of the spatial correlations determines the resolution of the imaging system, although this requirement can be alleviated by employing scanning approaches instead of wide-field imaging.

In addition to imaging, QIUL facilitates spectroscopy. In this application, spatial correlations are not necessary, but frequency correlations are essential. A meticulous design of the down-converted light source, along with the optical configuration, allows the optimization of a QIUL system for specific applications.

The primary advantage of these techniques is that the object's information is detected within the visible spectrum. For example, this allows for the replacement of complex and expensive IR detector technology, such as Mercury Cadmium Telluride (MCT) detectors, with standard Silicon detectors, which offer better efficiency and lower intrinsic noise without necessitating cryogenic detection.

2.1 Goals and challenges

The goals of this initial study are divided into three main activities:

- Assessing the resilience of our nonlinear interferometry-based quantum sensor to atmospheric turbulence, experimentally simulated through the introduction of a rotating phase plate inside the idler arm of the interferometer.

The goal of this experimental analysis is to identify critical factors that can help design potential solutions or mitigation strategies. The robustness of a QIUL imaging system in a momentum correlations configuration against atmospheric turbulence will be quantified. The metrics for the quantification of atmospheric effects will be the resolution of the generated image. Atmospheric turbulence is expected to disrupt the spatial correlations between signal and idler photons, thereby degrading image resolution. These results will help analyze the necessary changes in system design to improve robustness.

- Numerically simulating the impact of atmospheric losses on QIUL setups, in the high gain regime, achieved through seeding a standard low-gain nonlinear interferometer. Simulation of the losses in a real scenario is realized by modifying an already existing code developed by the IOF team for payload analysis in QKD protocols. This study assumes a source in the high gain regime to ensure that enough scattered photons contribute to the interference signal required for QIUL operation.

The goal of this study is to quantify the amount of scattered photons that can be collected back in the nonlinear crystal (NLC) under different altitude of the backscattered signal. Evaluating typical image properties such as the signal-to-noise ratio, with photon fluxes consistent with existing literature on high-gain QIUL, will help quantify the losses in the beam traveling through the atmosphere. Optimizing the parameters of the high gain source to ensure high visibility of the interference signal generated[1] [1] will help compare the performance of the proposed quantum sensors to currently employed classical devices.

- Feasibility study of QIUL sensing techniques for EO missions, addressing the results from the previous analyses compared to the needs of these missions and the state of the art. The goal of this study is to evaluate the performance of current EO instruments combined with QIUL techniques based on the results obtained from the previous analyses, integrated with a quantitative study on the footprint, payload, stability, and detection efficiency attainable by an optimized version of the proposed quantum sensor. This will help assess the feasibility of QIUL schemes for EO and identify the requirements that need to be achieved for such a system to be employed in real missions.

The study performed in the framework of the ULEO project includes several innovative elements that are addressed by identifying the potential risk they introduce to the feasibility of using

[1] M. I. Kolobov et al., J. Opt. **19** (2017) 054003

quantum sensing techniques for Earth observation missions. The challenges initially identified are the following:

- Atmospheric Turbulence. Atmospheric turbulence can destabilize the interferometric signal, introducing significant challenges to maintaining coherence in an interferometric system.

- High Losses. The long distances and atmospheric conditions introduce substantial losses in one of the interferometer arms, unbalancing the interferometer and affecting the quality of the information.

- Correlation Degradation. Atmospheric effects can destroy the correlations between signal and idler photons, impacting the resolution and precision of measurements.

- Delay Line Design. A design for a delay line in the arm of the interferometer that remains in orbit is required to match the length of the other arm, ensuring proper synchronization.

- Photon Pair Source in High Gain Regime. An optimal design for a photon pair source operating in the high gain regime is required to detect scattered signals effectively.

The initially identified risks and mitigations to be assessed are summarized in the Table 2.1.1.

Table 2.1.1 Summary of the initially identified risks and mitigations to be assessed

Risk Identifier	**Description**	**Likelihood**	**Severity**	**Mitigations to be assessed**
Atmospheric turbulence	The expected level of atmospheric turbulence for typical EO missions could potentially destroy the spatial correlations in the experimental analysis, necessitating a shift from an imaging approach to either a spectroscopy or a point image (scanning) approach for the potential implementation.	Medium	Low	-Implement adaptive optics (AO) to correct the scattered wavefronts. -Utilize a spatial light modulator (SLM) in the pump beam path within the interferometer to replicate the same turbulence profile experienced by the idler beam into the pump field. -Consider transitioning to a spectroscopy or point image (scanning) approach, where spatial

				correlations are not essential for the application.
Photon flux limitations	If the highest reported flux rate in a high gain regime of 10^12 pairs/s is insufficient to collect a signal after accounting for losses, alternative EO mission designs may need to be evaluated to leverage QIUL effectively.	Medium	Medium	-Explore mechanisms to compensate for the photon flux losses of the idler beam[2] -Assess alternative EO mission designs, potentially targeting slightly different applications. For instance, consider the advantages of a Satellite-Satellite approach instead of a Satellite-Earth link.
Mechanical stability	Deviations of the satellite from its orbit, including oscillations in satellite altitude and vibrations during operation, must be considered and compensated. The interferometer arms need to maintain equal length for the interference signal to be observed.	High	Low	-Integrate active stabilization elements into the interferometer design to actively compensate for mechanical instabilities.

The activities are divided into the different work packages shown in Fig. 2.1.1.

[2] M. I. Kolobov et al., J. Opt. **19** (2017) 054003

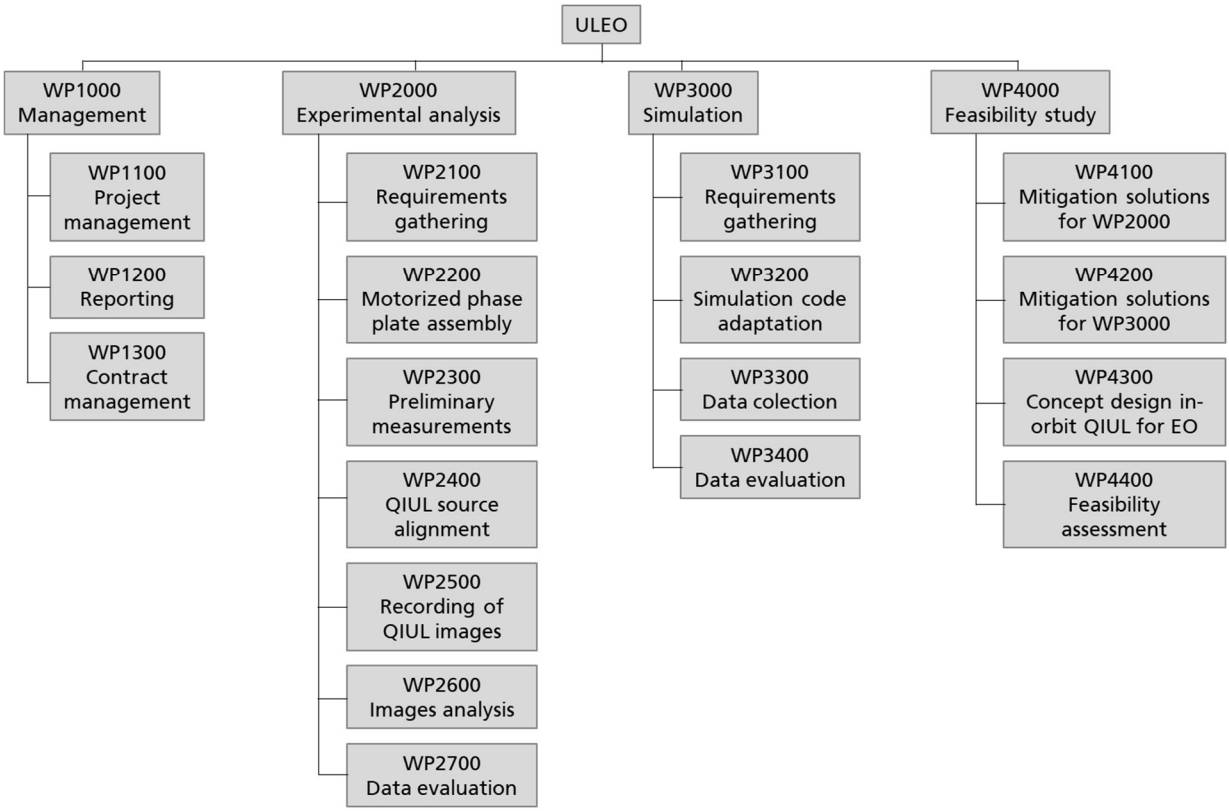

Figure 2.1.1 Diagram of the different ULEO workpackages and activities

3 PROGRESS REPORT

3.1 Baseline Schedule

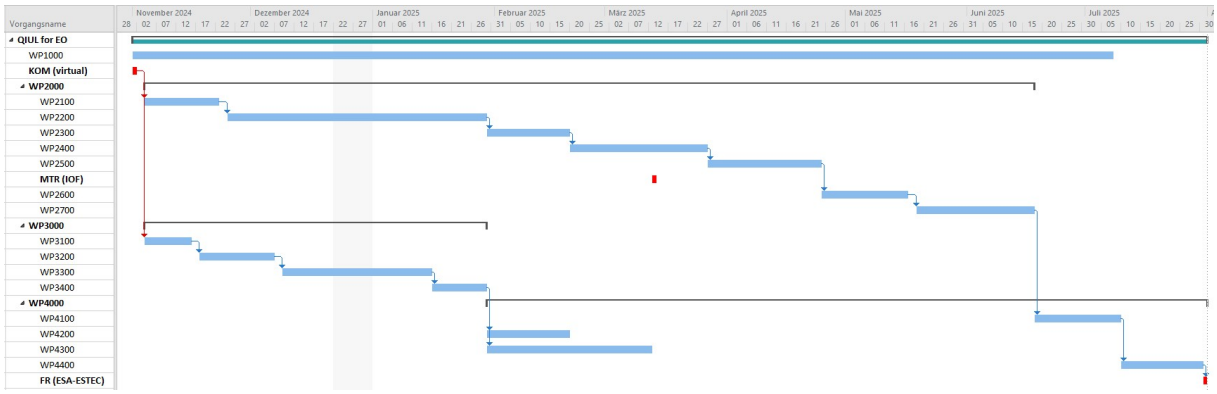

Figure 3.1.1 Proposed Gannt chart in the project proposal

Given the innovative nature of the study, the evaluation of the challenges and risks for different quantum sensing approaches (a part of WP4300 and WP4400) was agreed to be the initial activity of the project during the Negotiation Meeting on 04.10.2024. The idea behind this change was

to better evaluate the activities to be performed in the frame of the project, in order to maybe change the focus of the proposed activities in WP2000 and WP3000. On the Requirement Review Meeting (RRM) on 29.11.2024 the initial study was presented to ESA and discussed, and it was concluded to proceed with the proposed activities for the WP2000 and WP300. After the RRM, an updated Gantt chart was sent, which accounted for the initial study performed as part of WP2100 and WP3100 which are then extended in time. The new schedule in Fig. 3.1.2.

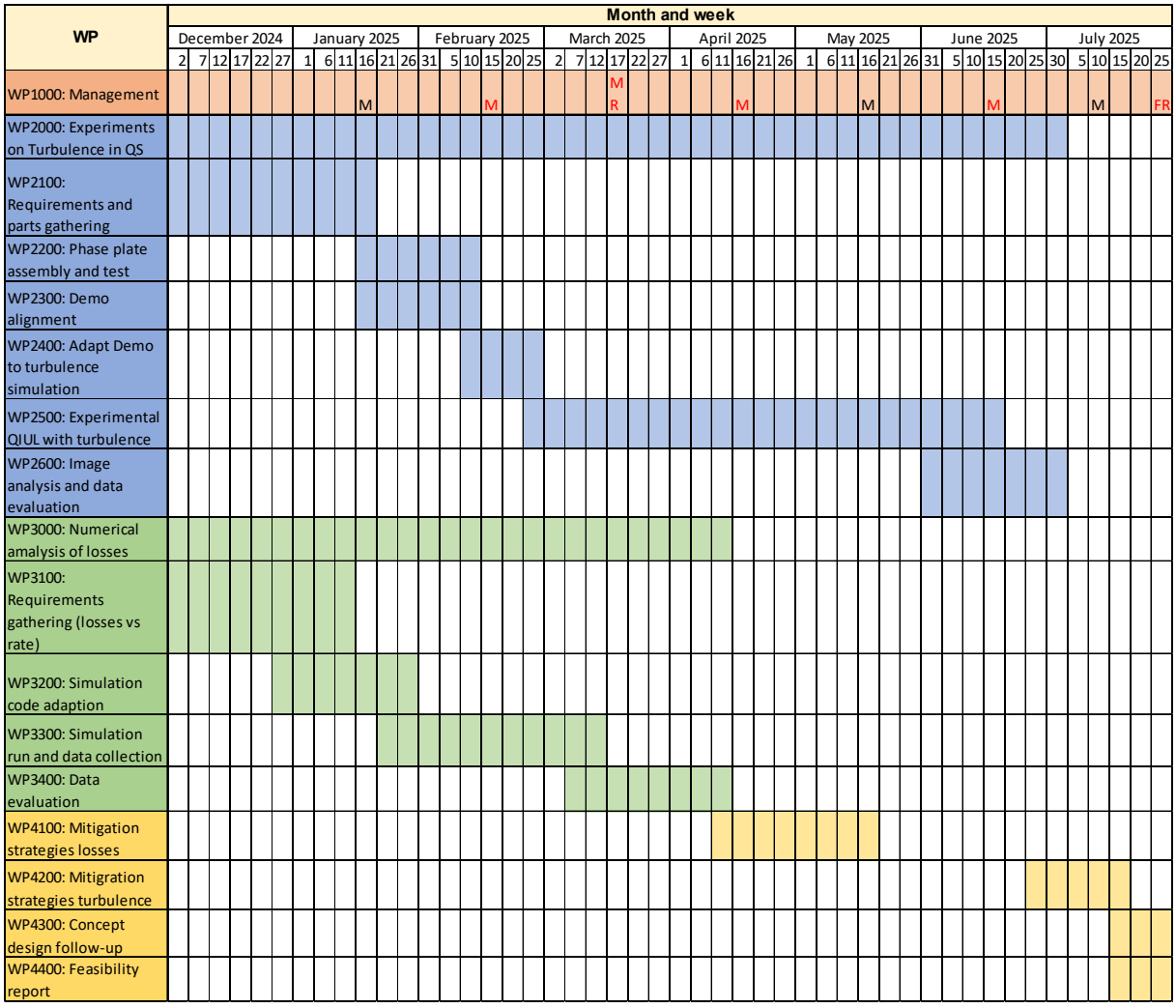

Figure 3.1.2 Gannt chart after the RRM meeting

3.2 Project meetings list

Meeting	Date	Place	Main outcomes	File name
Negotiation	04.10.2024	Online	Evaluation of the challenges and risks for different	2024-10-04_ULEO_Negotiation_F-IOF.pdf

			quantum sensing approaches as initial activity	2024-10-15_ULEO_Negotiation-Minutes_Draft_VFG FFi.pdf
Kick-off	05.11.2024	Online	Requirement review meeting necessary	ULEO_KickOff.pdf
Requirement Review	29.11.2024	Online	Agreed to proceed with the experiment on the effect of atmosphere turbulences on image quality	ULEO_RRM.pdf ULEO_Requirement_Review_Meeting_29112024_MoM_singed.pdf
Technical 1	15.01.2025	Online	Status update	ULEO_TM1.pdf
Technical 2	14.02.2025	Online	Status update. Phaseplates to simulate turbulences delivery date by 31.03.2025, expected duration of WP2000 until 15.07.2025	ULEO_TM2_WP2000.pdf ULEO_TM2_WP3000.pdf ULEO_Technical_Meeting_14022025_MoM_sign_JH.pdf
ULEO Workshop	27-28.03.2025	IOF, Jena	Quantum sensing approaches working principles overview Classical LIDAR approaches overview Quantum sensing model and parameters , and comparison to the classical models Status update and lab tour	ULEO_Workshop_032025.pdf
MTR	03.04.2025	Online	Turbulence phaseplates for WP2000 to be	ULEO_MTR.pdf ULEO_MTR_03042025_MoM_sign.pdf

			delivered by 04.04.2025	
Technical 3	07.05.2025	Online	Initial experimental results on resolution and SNR when turbulence is present, and the need to change acquisition technique to off-axis holography	ULEO_TM3.pdf
Technical 4	04.06.2025	Online	Final results on resolution and SNR when turbulence is present, to be presented at LPS25 conference	ULEO_TM4.pdf ULEO_Technical_Meeting_04062025_MoM_sign.pdf
Technical 5	01.07.2025	Online	Final report structure information from JH to IOF	
FR	23.09.2025	ESTEC, Noordwijk		

3.3 Contribution to Living Planet Symposium 2025

The contribution to the living planet symposium on 26.06.2025 is attached as part of the final documentation package as "1578_GilaberteBasset.pptx".

A comment that arose from the talk was that it would be interesting to also test the system performance when the turbulence is simulated close to Earth, instead of far from it which was the configuration presented. That triggered a set of second measurements on the effects of turbulence close to Earth on image resolution and SNR. Both measurements and results are reported in the present document, in Sec. 4.4.

4 PROJECT ACHIEVEMENTS

This chapter is dedicated to present the main findings of ULEO and it is organized in the following way:

- Section 4.1 explains the state-of-the-art on the proposed optical quantum sensing techniques and on widespread quantum light sources; we also mention IOF contribution to the state-of-the-art.
- Section 4.2 reports on the activities in WP2100 and WP3100, focusing on the identification of main challenges and risks.
- Section 4.3 also reports on activities in WP2100 and WP3100, highlighting the evaluation of a quantum advantage regime.
- Section 4.4 reports on the experimental activities performed in WP2200-WP2600.
- Section 4.5 reports on the numerical activities performed in WP3200-WP3400.
- Section 4.6 reports on possible risk mitigation strategies identified within WP4100-WP4200.
- Section 4.7 reports on a high-level possible mission concept design (WP4300).

4.1 Introduction to optical quantum sensing and state of the art on proposed methods

Optical quantum sensing protocols have been explored for over two decades, leading to groundbreaking technologies across various fields, including biomedicine, materials science, and chemistry, with promising future applications in space exploration[3]. Despite significant achievements, a broader perspective on quantum metrology reveals new opportunities for fundamental research and practical applications. In ULEO we identify two main branches of protocols, interference-based and correlation-based; the former has been investigated both numerically and experimentally, while the latter has been numerically addressed with the aim of a feasibility assessment for Earth Observation (EO) applications. Before introducing correlation- and interference-based optical quantum sensing protocols, we will introduce few relevant classes of quantum states of light, their properties, how they can be generated, and their relevance throughout this report.

Among the most popular quantum light sources, photon-pair sources find extremely wide application in quantum technologies, ranging from quantum communication, quantum computing and quantum sensing. To produce such states, typically second order- and third-order nonlinear optical processes are employed, namely Spontaneous Parametric Down-Conversion (SPDC) and Spontaneous Four-Wave Mixing (SFWM), respectively[4]. In both processes, one (SPDC) or two photons (SFWM) from a strong pump beam are converted into a photon pair exhibiting correlations in several degrees of freedom: spatial, time, momentum, frequency; these processes happen upon fulfilment of energy and momentum (also called phase-matching) conservation

[3] Genovese, M., Real applications of Quantum Imaging, J. Opt. 18, 073002 (2016).
[4] R. W. Boyd, "Nonlinear optics", Burlington: Academic Press, 3rd edition (2008).

laws, and can be engineered to control the photon-pair emission wavelengths, as well as their polarization, to generate polarization-entangled photon pairs. Photon-pair generation through SPDC is depicted in Fig. 4.1.1. While entanglement engineering of photon-pair sources is fundamental in quantum communication and quantum computing, the ability to control non-degenerate SPDC, in which one photon can be, e.g. in the NIR[5], MIR[6], THz[7], or UV[8], while its partner can be in the VIS, becomes important for optical quantum sensing purposes, exploiting frequency correlations for the employment of so-called "two-color" schemes. Additionally, photon-pair correlations grant a certain amount of resilience against detrimental effects such as turbulence, noise, and scattering.

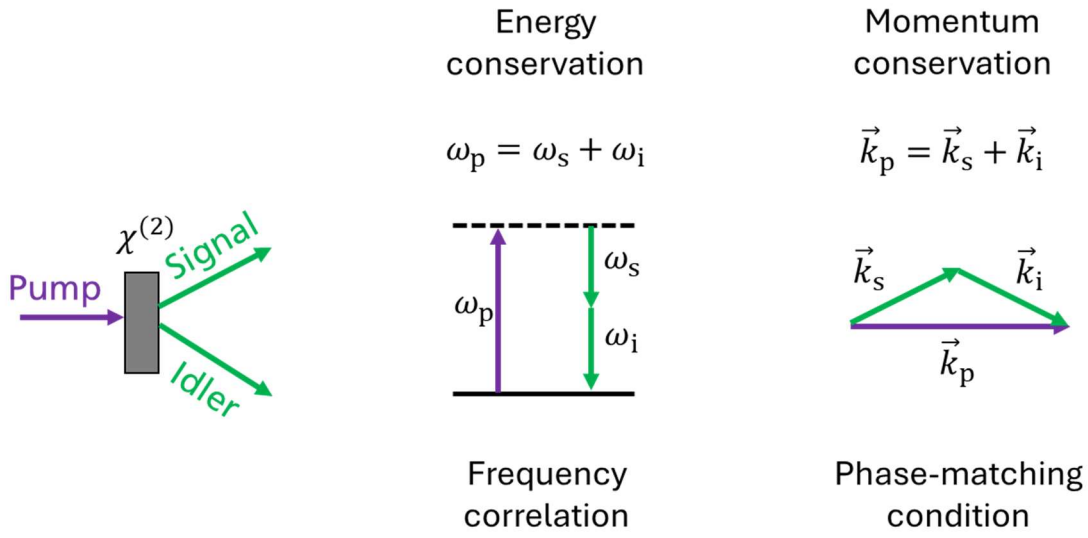

Figure 4.1.1 Sketch of photon-pair generation in SPDC. A strong pump laser impinges on a crystal with second-order ($\chi^{(2)}$) nonlinearity. For efficient pair generation, energy conservation and momentum conservation conditions must be satisfied.

A different class of quantum light sources is represented by single photon sources, defined as devices or materials capable of generating and emitting individual photons. The main feature and difference with photon-pair states lies in the ideally zero variance in photon number exhibited by such states[9]. They can be generated in practice based on various physical systems, such as quantum dots[10], 2D materials[11], heralded photon-pair sources, and even DNA-metal

[5] M. Hong, et al., Polarization-entangled photon-pair source using beam displacers and thin crystals, Opt. Lett. 49, 5467-5470 (2024).
[6] M. Kumar, et al., Mid-infrared photon pair generation in $AgGaS_2$. Appl. Phys. Lett. 119 (24): 244001 (2021).
[7] M. Kutas et al., Terahertz quantum sensing. Sci. Adv.6,eaaz8065(2020).
[8] P. Goswami et al., arXiv preprint arXiv:2505.13721 (2025).
[9] R. Loudon, The quantum theory of light. OUP Oxford (2000).
[10] N. Somaschi, et al. Near-optimal single-photon sources in the solid state, *Nature Photonics* 10.5, 340-345 (2016).
[11] P. Tonndorf, et al. Single-photon emission from localized excitons in an atomically thin semiconductor, Optica 2.4, 47-352 (2015).

nanoparticles[12]. For quantum sensing purposes, protocols for spectroscopy[13] or transmission[14] measurements employing single photon sources have been shown to provide quantum-enhanced sensitivity compared to classical sources. Despite the potential for applications, such quantum advantage is extremely fragile against optical losses; when these exceed 50%, calculated from source to detection, all quantum advantage vanishes, making the applicability of such sources to EO impractical.

Squeezed light sources are specialized optical devices that produce light with reduced quantum fluctuations in one of their properties, typically the amplitude or phase, compared to standard coherent light sources. This phenomenon, known as "squeezing," allows for improved precision in measurements and enhanced performance in various applications, such as quantum microscopy[15], gravitational wave detection[16], and quantum information processing[17]. Squeezed light is generated through non-linear optical processes, such as SPDC or SFWM in the so-called "high-gain regime"[18]. This applies to very strong pump regimes (typically reached with picosecond pulse lasers), such that not just a single photon-pair is generated through the nonlinear process, but multiple photon-pair contributions become relevant, or seeded SPDC (Fig 4.1.2). The peculiarity of this quantum state of mind lies in the possibility to manipulate it to achieve lower noise levels in one degree of freedom (also called quadrature), while increasing noise in the complementary quadrature. This unique property enables significant advancements in sensitivity and accuracy for experiments that rely on the quantum nature of light. As for single-photon states however, such quantum enhancements in sensitivity and noise reduction is extremely fragile to losses, making such kind of quantum advantage not pursuable for EO applications. Nevertheless, over the course of ULEO, we considered Squeezed light generated through the high-gain regime of SPDC with the purpose of reaching photon fluxes comparable to classical active LIDAR missions, while focusing on a detection efficiency quantum advantage enabled by two-color optical quantum sensing protocols. The Photonic Quantum Systems department at Fraunhofer IOF possesses a longstanding experience in the development of custom high-performance quantum

[12] M. Busson, et al, Accelerated single photon emission from dye molecule-driven nanoantennas assembled on DNA, Nat. Commun. 3, 962 (2012).
[13] R Whittaker et al, Absorption spectroscopy at the ultimate quantum limit from single-photon states, New J. Phys. 19 023013 (2017).
[14] E. Jakeman E and J. G. Rarity, The use of pair production processes to reduce quantum noise in transmission measurements, Opt. Commun. 59 219 (1986).
[15] R. B. de Andrade, et al., Quantum-enhanced continuous-wave stimulated Raman scattering spectroscopy, Optica, 7, 470, 2020.
[16] The LIGO scientific collaboration, Enhanced sensitivity of the LIGO gravitational wave detector by using squeezed states of light, Nat. Phot., 7, 613, 2013.
[17] C. S. Hamilton et al., Gaussian Boson Sampling, Phys. Rev. Lett. 119, 170501 (2017).
[18] K. Hashimoto, et al., Broadband spectroscopy and interferometry with undetected photons at strong parametric amplification, Advanced Quantum Technologies 8.4, 2300299 (2025).

light sources for quantum communication[19,20], integrated sources[21], non-degenerate sources in the NIR[22] and in the UV[23] for two-color quantum imaging.

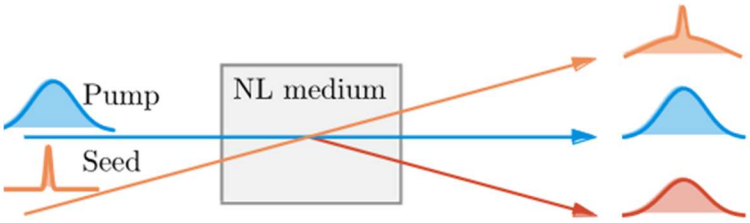

Figure 4.1.2 One strategy for squeezed light generation: seeded SPDC. Differently from low-gain SPDC, a seed laser impinges on a nonlinear (NL) crystal together with the pump.

Optical quantum sensing based on photon-pair correlations has been investigated for about 30 years now[24]. Historically, imaging has been the first application being tackled, thus the imaging protocol using quantum correlations has been called "Quantum Ghost Imaging" (QGI), and was first realized by exploiting quantum correlations of photon pairs generated through the process of SPDC; it is defined in the following way[25]:

- A laser pump (either continuous wave or pulsed) generates photon pairs through SPDC by illuminating a nonlinear crystal.
- The photon pairs get spatially separated into two paths; one of them interacts with the target to be imaged, where the reflected or transmitted signal is collected by a detector with a large numerical aperture but without the ability to spatially resolve the detected field, the so-called bucket detector.
- The other photon is instead directly imaged by a spatially resolving detector. Neither of the two measurements alone contains enough information to reconstruct the image.
- Measuring the photon correlations, i.e. for QGI measuring spatially resolved coincident events between the bucket detector and the camera, allows to retrieve the image.

The protocol is visualized in Fig. 4.1.3. It must be noted that quantum correlations are not a necessary condition to perform QGI; after the first demonstration in 1995 it was later discovered that other classes of classical light sources exhibiting non-trivial correlations also enabled ghost

[19] R. Fazili, et al., Simple but efficient polarization-entangled photon sources, J. Opt. Soc. Am. B 41, 2692-2701 (2024).
[20] E. Brambila, et al., Ultrabright polarization-entangled photon pair source for frequency-multiplexed quantum communication in free-space, Opt. Express 31, 16107-16117 (2023).
[21] P. Hendra et al., Rubidium-Doped $KTiOPO_4$ Waveguides as a Dual-Type Photon Pair Source, arXiv preprint arXiv:2505.14269 (2025).
[22] M. Hong et al., Polarization-entangled photon-pair source using beam displacers and thin crystals, Opt. Lett. 49, 5467-5470 (2024).
[23] P. Goswami et al., Non-degenerate SPDC photon-pair source for UV-A illumination, arXiv preprint arXiv:2505.13721 (2025).
[24] T. B. Pittman, et al., Optical imaging by means of two-photon quantum entanglement, Phys. Rev. A 52, R3429 – R3430 (1995).
[25] J. H. Shapiro and R. W. Boyd, The physics of ghost imaging, Quantum Inf. Process. ed., 11, 949–993 (2012).

imaging, namely pseudo-thermal[26], true thermal[27], and modulated coherent sources[28]. Compared to classical Ghost Imaging, QGI however still retains a two-fold "quantum advantage":

- Enhanced Signal-to-Noise ratio[29], enabled by the possibility to filter uncorrelated events from correlated ones; this concept relies on the same physics of the so-called "Quantum Illumination"[30]; the same physical process of correlation-enabled filtering allows for image distillation[31] from noisy sets, even when noise levels are 10 times higher than the wanted signal.
- The possibility to perform "two-color" imaging; given the possibility to tune the wavelength of the generated SPDC photon pair, the photon interacting with the object can be designed to be in a wavelength range where detection technology is underdeveloped compared to VIS silicon CMOS detectors, but where single photon detector technology is still reasonably developed, such as the NIR[32]. Its partner photon, which is directly imaged onto the camera, can instead be designed to be in the VIS, benefitting from more advanced technological state-of-the-art. While MCT-based detectors also rely on silicon CMOS readout, they remain more complex and suffer from higher dark currents than VIS CMOS detectors. For this reason, QGI in the infrared needs an IR single photon detector, and a VIS camera, potentially offering a significant advantage to direct imaging, where an IR camera is needed.

In recent years, the development of SPAD array technology for the spatially resolved detection consistently advanced the state-of-the-art of QGI, with significant advancements towards 3D microscopy[33], 3D ranging[34], and sub-minute NIR imaging[35]. Specifically for its LIDAR application, QGI represents a possible candidate for EO purposes, given the extensive literature on the resilience of this scheme against turbulence[36] and scattering[37], together with the ability to perform imaging in turbid media[38] and exploit quantum correlations for adaptive optics purposes, correcting distortions in propagating wavefronts without the need of guide stars[39]. Within the

[26] A. Gatti, et al., Ghost imaging with thermal light: Comparing entanglement and classical correlation, Phys. Rev. Lett., 93, 93602 (2004).
[27] D. Zhang, et al., Correlated two-photon imaging with true thermal light, Opt. Lett., 30, 2354–2356 (2005).
[28] R. S. Bennink, et al., "Two-photon" coincidence imaging with a classical source, Phys. Rev. Lett. 89, 113601 (2002).
[29] J. H. Shapiro and R. W. Boyd, The physics of ghost imaging, Quantum Inf. Process. ed., 11, 949–993 (2012).
[30] S. Lloyd, Enhanced Sensitivity of Photodetection via Quantum Illumination, Science 321,1463-1465 (2008).
[31] H. Defienne et al., Quantum image distillation. Sci. Adv.5,eaax0307(2019).
[32] R. S. Aspden, et al., Photon-sparse microscopy: visible light imaging using infrared illumination, Optica 2, 1049–1052 (2015).
[33] A. Eshun, et al., 3D quantum ghost imaging microscope, Optica 12, 1109-1112 (2025).
[34] C. Pitsch, et al., 3D quantum ghost imaging, Appl. Opt. 62, 6275-6281 (2023).
[35] V. F. Gili, et al., Quantum ghost imaging based on a "looking back" 2D SPAD array, Appl. Opt. 62, 3093-3099 (2023).
[36] P. B. Dixon, et al., Quantum ghost imaging through turbulence Phys. Rev. A 83, 051803(R) (2011).
[37] W. Gong and S. Han, Correlated imaging in scattering media, Opt. Lett. 36, 394–396 (2011).
[38] M. Bina, et al., Backscattering differential ghost imaging in turbid media, Phys. Rev. Lett. 110, 083901 (2013).
[39] P. Cameron et al., Adaptive optical imaging with entangled photons, Science383,1142-1148 (2024).

Fraunhofer IOF team, we possess expertise in this optical quantum sensing protocol, testified by two scientific publications in international, peer-reviewed journals[12,40].

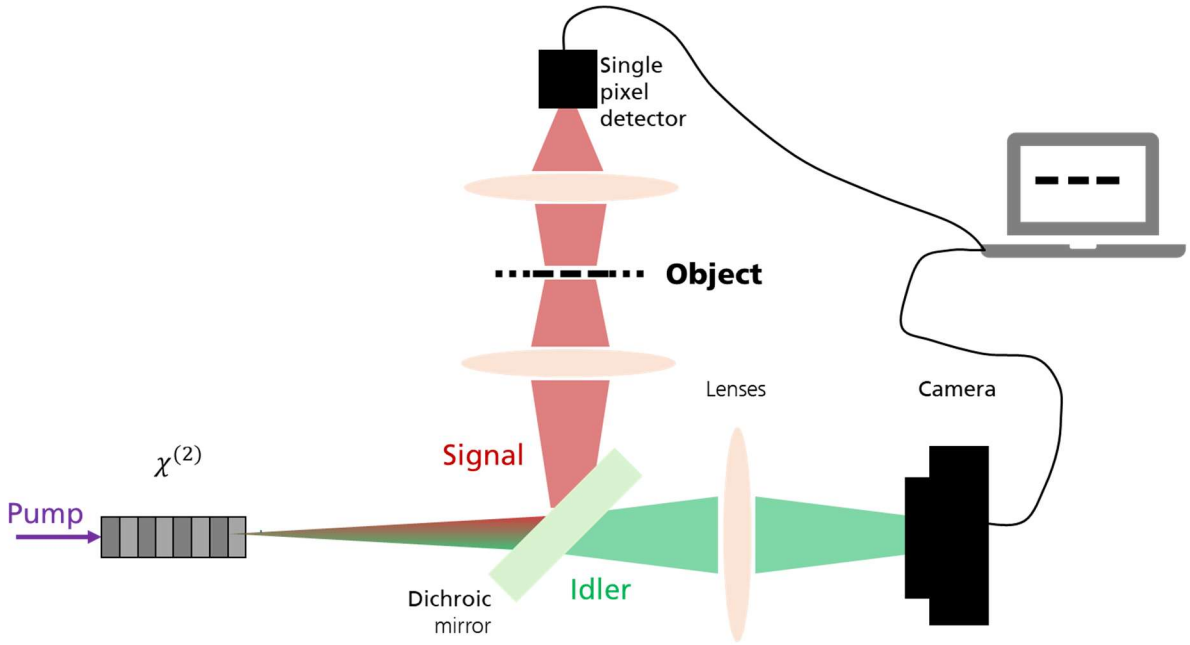

Figure 4.1.3 Schematics of the Quantum Ghost Imaging technique. Photon-pairs are generated through SPDC; assuming a non-degenerate process, signal and idler photons can be separated with a dichroic mirror and propagated in two different paths. The signal path contains the object to be imaged, and signal light is collected by a single pixel detector with no spatial resolution. The idler path directly images the crystal plane onto a camera. Neither of the two measurements alone contain enough information to reconstruct the object; this can only be performed via correlating the camera and single pixel detector measurements.

A more recent protocol for optical quantum sensing, named Quantum Imaging with Undetected Light (QIUL) has been established and thoroughly investigated over the past decade. Such approach builds on seminal works, dating back to the early 90´, on the fundamentals of nonlinear interferometers, induced coherence, and their connection to the quantum mechanical wave-particle duality[41,42].More than 20 years later, it was finally discovered that such physical system can be employed for imaging[43], giving rise to the QIUL field. Physically, this phenomenon is enabled when nonlinear crystals are embedded in interferometers (commonly nonlinear Mach-

[40] M. Braasch et al., Classical Ghost Imaging: A Comparative Study of Algorithmic Performances for Image Reconstruction in Prospect of Plenoptic Imaging, IEEE Photonics Journal, 13(3), 6800914 (2021).
[41] Zou, X. Y., Wang, L. J. & Mandel, L. Induced coherence and indistinguishability in optical interference. Phys. Rev. Lett. 67, 318–321 (1991).
[42] Wang, L. J., Zou, X. Y. & Mandel, L. Induced coherence without induced emission. Phys. Rev. A 44, 4614–4622 (1991).
[43] G. Lemos, et al., Quantum imaging with undetected photons, Nature 512, 409–412 (2014).

Zehnder and Michelson interferometers); they are aligned such that the "which-path" information of the undetected beam, or idler beam, is erased, meaning that a hypothetic observer measuring the idler beam would not be able to distinguish whether the photon comes from the first or the second SPDC process. This indistinguishability induces coherence between the signal and idler beams, resulting in interference observed in the signal beam. Any target information encoded in the idler path (introducing which-path information) would then be coherently transferred to the signal beam. After the first imaging demonstration, the approach has been adapted in general to several optical sensing scenarios[44], including holography[45], birefringence and diattenuation sensing[46], spectroscopy[47], ranging[48], gas sensing[49], and quantum state tomography[50]. Thanks to the decoupling of the sensing and detected beams, "two-color" schemes have also been implemented with the QIUL protocol, where the main difference compared to QGI is now that not even a bucket detector for the more "exotic" wavelength range is needed; this is reflected by the fact that QIUL has been demonstrated beyond the NIR, in more challenging spectral regions regimes, such as the MIR[51] and THz range[52], with VIS detection. While the available sensing configuration is a wide-field system for most implementations, a MIR scanning approach has also been developed at IOF[53]. Unlike QGI however, the literature lacks a study on the potential resilience of this approach against atmospheric turbulence. A final difference with the correlation-based protocol lies in its adaptability to the high-gain regime; in addition to higher photon fluxes, this regime might allow high values of visibility independently of atmospheric losses by carefully compensating for them[54]. Spectroscopy in the high gain regime has been recently reported[55]. Fraunhofer IOF possesses consistent experience in the QIUL protocol; aside the above-mentioned MIR scanning microscopy work, the Quantum Sensing and Imaging group was the first to demonstrate this technique with compact Michelson geometries, with video-rate imaging performances and high interferometric stability[56]. The QIUL technique, in both its Michelson and Mach-Zehnder configurations is depicted in Fig. 4.1.4. Additional relevant studies conducted by

[44] J. Fuenzalida et al., Nonlinear interferometry: A new approach for imaging and sensing, Adv. Quantum Technol. 7, 2300353 (2024).
[45] S. Töpfer et al., Quantum holography with undetected light, Sci. Adv. 8, eabl4301(2022).
[46] C. Oglialoro, and E. Giese, Sensing Birefringence and Diattenuation with Undetected Light, arXiv:2505.02732 [quant-ph] (2025).
[47] C. Lindner, et al., Fourier transform infrared spectroscopy with visible light, Opt. Express 28, 4426-4432 (2020).
[48] G. Qian et al., Quantum Induced Coherence Light Detection and Ranging, Phys. Rev. Lett. 131, 033603 (2023).
[49] J. Dong et al., Open-Path Methane Sensing via Backscattered Light in a Nonlinear Interferometer, arXiv:2506.17107 [physics.optics] (2025).
[50] J. Fuenzalida et al., Quantum state tomography of undetected photons Phys. Rev. A 109, 022413 (2024).
[51] I. Kviatovsky et al., Microscopy with undetected photons in the mid-infrared, Science Advances, 6, 42, eabd026, (2020).
[52] M. Kutas et al. Terahertz quantum sensing, Sci. Adv. 6, 11, eaaz8065 (2020).
[53] J. R. Léon Torres et al., Mid-infrared quantum scanning microscopy via visible light beyond spatial correlations, arXiv:2505.04490 [physics.optics] (2025).
[54] M. I. Kolobov et al., Controlling induced coherence for quantum imaging, J. Opt. 19, 054003 (2017).
[55] K. Hashimoto et al., Fourier-transform infrared spectroscopy with undetected photons from high-gain spontaneous parametric down-conversion, Commun. Phys. 7, 217 (2024).
[56] M. Gilaberte Basset, et al. Video-Rate Imaging with Undetected Photons, Laser & Photonics Reviews 15.6, 2000327 (2021).

IOF included a fundamental work on resolution limits[57], the extension of this quantum sensing protocol to phase imaging[58,59], and the demonstration f noise resilience through distillation[60].

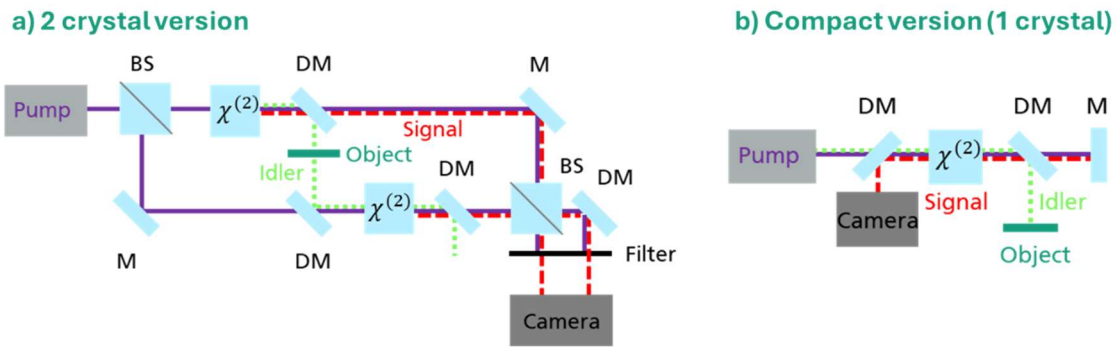

Figure 4.1.4 Principle of the QIUL protocol. a) 2-crystal version of the technique; 2 identical nonlinear crystals are embedded in a Mach-Zehnder interferometer, both generating photon pairs from a strong laser pump. When signal, idler and pump paths are indistinguishable, such that a camera cannot identify which signal photons were generated from the first crystal and which from the second one, induced coherence occurs. Thus, information on an object in the idler path between crystals 1 and 2 can be coherently transferred to signal photons, and detected by the camera in the scheme, without having to detect the idler photons which directly interacted with the object. Hence the name imaging with undetected photons. b) compact one-crystal Michelson QIUL setup. Here a single nonlinear crystal is needed, simplifying the setup and increasing the interferometer stability; the physical principle is identical to the 2-crystal version.

4.2 WP2100, WP3100: Evaluation of the challenges and risks for different quantum sensing approaches as initial activity

Two main quantum sensing techniques are addressed: correlation-, and interference-based sensing. Both techniques can run in different modalities depending on the application: wide-field imaging, scanning imaging, spectroscopy, and time of flight measurements. There are common challenges identified for both techniques in order to make them suitable for space applications, and few challenges that are specific depending on the technique used.

For a correlation-based sensing scenario, the main drawback is that the probe wavelength still needs to be detected. Therefore, not introducing a clear advantage for Earth observation

[57] M. Gilaberte Basset et al., Experimental analysis of image resolution of quantum imaging with undetected light through position correlations, Phys. Rev. A 108, 052610 (2023).
[58] S. Töpfer et al., Quantum holography with undetected light, Sci. Adv. 8, eabl4301(2022).
[59] J. R. León-Torres et al., Off-axis holographic imaging with undetected light, Opt. Express 32, 35449-35461 (2024).
[60] J. Fuenzalida et al., Experimental quantum imaging distillation with undetected light, Sci. Adv. 9, eadg9573 (2023).

applications in terms of reducing the payload of the satellite by replacing IR by visible detectors. For this reason, this project mainly focuses on interference-based techniques. However, correlation-based techniques could enhance the SNR of the images obtained compared to what would be achievable with classical approaches.

For an interference-based sensing scenario, the main challenge is to maintain the indistinguishability between the forward and backward generated idler (or probe) beams. The reason for this will be more carefully introduced in Section 4.4. Nevertheless, this is an engineering challenge that we believe does not risk the feasibility of this technique for Earth observation applications.

The main challenges that would have to be addressed for both techniques can be classified as effects related to atmospheric turbulences, the intensity of the returned signal, and to altitude measurements.

The implication of each of these challenges has been addressed, as well as the criticality that it imposes on the different sensing approaches, at the beginning of the project. The aim of this initial study is to get a better overview of the more critical points which would need to be addressed first to evaluate the feasibility of quantum sensing techniques for Earth observation. Table 4.2.1 summarizes the result of this initial study.

Table 4.2.1. Overview of the main critical challenges identified for each quantum sensing approach as possible techniques for Earth observation. The colors indicate the criticality of the risk (green= not affected, yellow=medium impact or easy solution, red=big impact or challenging solution).

CHALLENGES		QUANTUM SENSING APPROACH			
		Wide-field imaging and sensing	**Point scan sensing**	**Spectroscopy**	**Correlation-based imaging and sensing**
Atmospheric turbulence	Loss of spatial correlations	If no spatial correlations, no spatial resolution, maybe compensated by AO	Single pixel approach, not afected by spatial correltations loss. Probably bad resolution due to big FOV at ground, maybe still useful. Maybe slow.	Based on frequency correlations, no need of spatial resolution to get composition information. Scattering and dispersion, can be either seen as losses or the quantity to measure depending on the application	If in single pixel approach, no need for spatial correlations. If wide-field, spatial correlation needed. Plenoptic imaging approach might fail
	Wavefront distortion and scintillation: decrease indistinguishability and strength of spatial correlations	Loss of visibility , spatial resolution, and SNR. Partically corrected by AO Possible solution: synthetic off-axis technique	Not afected by spatial correltations loss, but loss of visibility and therefore lower SNR		Decrease of spatial correlations strength
	Decoherence	Decrease of visibilitiy, no interference possible if temporal decoherence is bigger than coherence time of the SPDC. Exact effect needs to be further studied, to maybe identify possible solutions			Destroy time correlations, no coincidence measuerement possible. Exact effect needs to be further studied, to maybe identify possible solutions

Altitude measurements	Altitude resolution	Depends on the bandwidth of the generated light (the wider bandwidth, the better axial resolution) BUT also, the more sensitive to the altitude instabilities of the satellite and to temporal decoherence effects. However, the stability of a Sagnac-loop source developed at Fraunhofer IOF is already tested for space applications [1]. An alternative to controlling the bandwidth of the generated light is strong focusing to have a high axial resolution, but the focusing plane must be adaptable for each heigh plane. Related to the NA of the optics involved (low NA, lower axial resolution).	
	Altitude measurement stability	Depends on the satelite orbit stability, and requires an active compensation by the delay arm	
	Delay arm length	The interferometer arms that stay in the satellite have to be same length as probe arm (satellite to earth distance). Therefore a delay solution is needed for the interferometer arms in the satellite. This solution might be either fiber based or free-space (e.g. Herriot cells).	The delay solution might be an electronic dely on the detector side. But it might become very slow to compensate for long distances. Maybe as a solution for a fine tunning for the delay line.
	Scanning of delay arm	The length of the scanning range determines the range of heights than can be measured. The longer the scanning range, the more height range we can measure. Needs to be fast and active tunable to compensate for satellite instabilities or change in surface heigth. Coarse alignment (to set the altitude plane) and fine adjustment (to compensate for smaller changes in height)	The delay solution might be an electronic dely on the detector side. But it might become very slow to compensate for long distances. Maybe as a solution for a fine tunning for the delay line.
	Changing ground height	If height change in ground is bigger than coherence length of the spdc, it would cause the interference to vanish if the delay arm is fixed. A system to scan the delay arm to cover the expected height changes is needed. Scanning system has to be fast enough to detect the changes. The length that delay line has to move to retrieve interference again, would be used to calculate height changes (similar to a time-of-flight measurement).	The delay solution might be an electronic dely on the detector side. But it might become very slow to compensate for long distances. Maybe as a solution for a fine tunning for the delay line.
	Different ground height within focal point	Effect depends on the altitude resolution. If the height change is bigger than coherence length, interference will be lost for a fixed position of the delay arm. The better the height resolution, the worse effect a height change will have on the interference detection and it'll have to be carefully controlled by the scanning of delay line	

Return signal to satelite	Background/Noise signals	Background and noise lower SNR, but these signals might distilled from quantum signal			
	Daylight operation (distillation limit?)	Experimentally demonstrated a 1:250 ratio, theory predicted 1:5000 for a system like in [2]			Experimentally demonstrated that 20x bigger noise intensity than quantum signal can still be distilled [3]
	Strength of return signal	Low strength of return signal implies low SNR and visibility. Visibility might be compensated (up to a limit) by lowering the intensity of the beam in delay line accordingly (long exposure time) because high visibility needs indistinguishability. Higher signal for single-pixel approaches (scanning/spectroscopy). Possible solution: high-gain regime	Low SNR but better than wide-field because signal is concentrated into a smaller detection region. Possible solution: high-gain regime	Low SNR but better than wide-field because signal is concentrated into a smaller detection region. Possible solution: high-gain regime	Low strength of return signal implies low SNR and heralding efficiency. Heralding efficiency might be compensated (up to a limit) by lowering the intensity of the beam in delay line accordingly (long exposure time). Possible solution: high-gain regime
	Scattering and absorption	Singal loss sources if it happens outside the probing area. Maybe synthetic wavelength approach as solution.			
	Depolarization (ground depolarization)	Decrease of indistinguishability. Increasing noise, lowering SNR			Might not affect since we only detect intensity counts
	Polarization scrambling	Decrease of indistinguishability. Possible solution: fast polarization scan on the reference arm (VIS). Demonstrated in the IOF group for quantum communications applications [4]			Might not affect since we only detect intensity counts
Others	Multispectral imager, measurement time for scanning different wavelengths considering ground speed of 7200m/s	Illumination wavelength can be tuned over a certain range (depending on spdc process) by changing temperature or angular orientation of the nonlinear crystal. Assuming 100ms acquisition time per image, minimum distance between images =720m. But even longer integration times might be necessary, and the time to tune the wavelength, even if fast, has to be considered. Broadband sources: microring resonators	Might be too slow for an image, but one could let the scanning mechanism to just be the staellite's footprint on Earth. Broad sources: microring resonators	Illumination wavelength can be tuned over a certain range (depending on spdc process) by changing temperature or angular orientation of the nonlinear crystal. Few ms per probing point. The acquisition time, together with the time to change probing wavelength, will affect the minimum distance between probed areas. Broadband sources: microring resonators	Coincidence measurement might be too slow, longer acquisition times than interference-based schemes [5]
	Optics to perfectly overlap the return signal to the backwards generated beam	Backreflected signal needs to perfectly overlap the backwards generated signal			No overlapping necessary
	Probing wavelength detector	No need to detect			Bucket detector needed

[1] ESA Space-EPS project (Photonic Transceiver for Secure Space Communications: New Space Suitable Entangled Photon Source), Call: ARTES 5.2 Call AO/1-6000/ 09/NL/US, rev. 7
[2] J. Fuenzalida et al., Sci. Adv. **9**, eadg9573 (2023)
[3] T. Gregory et al., Sci. Rep. **11**, 21841 (2021)
[4] Parab, T., 2025. A predictive polarisation compensation method for dynamic free-space optical links in quantum communication. Jena. https://doi.org/10.22032/dbt.67430
[5] V. F. Gili et al., Appl. Opt. **62**, 3093-3099 (2023)

In the frame of the ULEO project, we address several of the different identified challenges in different ways:

- experimentally: the atmospheric turbulence effects of wavefront distortion, loss of spatial correlations, scintillation (change of the intensity distribution on the beam), and decoherence on the image quality.
- simulation: losses due to backscattering, absorption, depolarization, to assess the amount of returned signal to the satellite and signal to noise ratio (SNR) expected for both, interference- and correlation-based scenarios.

- qualitatively: literature review on solutions for delay line techniques and feasibility, and a possible mission concept.

4.3 WP2100, WP3100: Evaluation of the quantum advantage

As mentioned briefly in the introduction, the primary advantage of the quantum sensing techniques proposed in this project is that the object's information is detected within the visible spectrum while the object itself is probed by a different wavelength, e.g. MWIR or LWIR. By shifting the detection wavelength from IR regimes to the visible, complex and expensive IR detector technology, such as Mercury Cadmium Telluride (MCT) detectors, can be replaced by standard silicon detectors, which offer better efficiency and lower intrinsic noise. The simplification of detection technology requirements could significantly impact the satellite payload for Earth observation missions that require the use of wavelengths for which no silicon detectors are feasible.

A more detailed comparison allowed to quantitatively compare the better performance of detection on the visible while detecting IR and visible light by checking some key features for different detectors: single photon detectors (SPDs), complementary metal-oxide-semiconductor (CMOS) cameras, and mercury-cadmium-telluride (MCT) detectors.

For SPDs, not only the single photon detection efficiency and dark counts affect the performance of the detection, but also the timing resolution and dead time are relevant parameters that can limit the measurement capabilities. Table 4.3.1 collects and compares the parameters of different SPDs on the market for 1640nm (SWIR range) and 530nm (VIS range) detection wavelengths.

Table 4.3.1 Comparison between the parameters of different SPDs on the market for 1640nm (SWIR range) and 530nm (VIS range) detection wavelengths.

SPD	Single photon detection efficiency	Dark count	Dark count variation at ct. T	Single photon timing resolution	Output pulse width	Dead time	Operation temperature
IR IDQ[1] @ 1640nm	~10%	6000cps		150ps	100ns	10us	10 to 30°C
IR MPD[2] @1640nm	~15%	250cps		70-200ps		>40us (hold-off time)	-48 to -30°C
VIS Excellitas[3] @532nm	~50%	<1500cps	+-10%	350ps @825nm	10-28ns	22-42ns	5 to 70°C
VIS IDQ[4] @500nm	~35%	<7cps		<40ps	9-15ns	<45ns	Room temperature

[1]https://marketing.idquantique.com/acton/attachment/11868/f-f9bb7e76-6463-42f1-81f3-25245e96401b/1/-/-/-/-/2019%2007%20ID221%20Brochure.pdf
[2] https://photonics.laser2000.co.uk/wp-content/uploads/2021/07/PDM-IR-Datasheet-Fiber.pdf
[3] https://www.excelitas.com/de/de/file-download/download/public/60241?filename=Excelitas_SPCM-AQRH_Family_datasheet.pdf
[4] https://marketing.idquantique.com/acton/attachment/11868/f-0236/1/-/-/-/-/ID100_Brochure.pdf

From the examples in this table, it is clear that VIS SPDs outperform the SWIR detectors in terms of single photon efficiency, dark counts, dead times, and in some cases even in timing resolution. Here it is important to note the difference between dead time and hold-off time (parameter given for the IR MPD detector in the table): dead time = time it takes to quench the avalanche + time to reset the detector to its initial state. Hold-off time: portion of the dead time that is introduced after the quenching process to avoid after pulsing.

While EO missions often use avalanche photodiodes (APDs) rather than SPDs, our focus here is on scenarios where the return signal is very weak and SPDs offer a clear advantage. For applications with higher return flux, commercial APDs promise high quantum efficiency (QE >70%) for wavelength up to 1600nm and rapidly decreasing afterwards[61]. Despite this, visible APDs still achieve superior efficiencies, with QE exceeding 90%[62].

[61] https://www.lasercomponents.com/fileadmin/user_upload/home/Datasheets/lc-apd/iag-series-ingaas-apd.pdf
[62] https://www.lasercomponents.com/fileadmin/user_upload/home/Datasheets/lc-apd/sar-series.pdf

Having in mind wide-field imaging applications, a comparison between CMOS cameras on the market to image in the SWIR and VIS ranges is presented in the Table 4.3.2.

Table 4.3.2 Comparison between the parameters of different CMOS cameras on the market for 1640nm (SWIR range) and 530nm (VIS range) detection wavelengths.

Camera type	QE	Frame rate	Pixel size	Area	Readout noise	Dark current	Operation temperature
CMOS Sony[1] @ 1640nm	~60%	70-173fps	3,45-5um	656x520px 2080x1544px	<200e- rms	<12ke-/s	
SWIR Andor[2] @1640nm (up to 2150nm)	>70%	600fps		640 x 512px	40e- rms	20,5-210 ke-/pixel s	-55°C
sCMOS Photometrics[3] @532nm	>90%	43,5-63fps	6,5um	2048x2048px	1.1e- rms	0,5e-/pixel s	-20°C

[1] requested information to Sony, https://www.sony-semicon.com/en/products/is/industry/swir/imx992-993.html
[2] https://andor.oxinst.com/products/swir-cameras-for-physical-science-and-astronomy
[3] https://www.teledynevisionsolutions.com/de-de/products/prime-bsi/?vertical=tvs-photometrics&segment=tvs

From the examples in this table, VIS range cameras have lower noise and dark current while having higher quantum efficiency.

For more extreme probing wavelengths, MCT detectors are typically the preferred detector since they cover longer wavelength IR ranges. For this scenarios, Table 4.3.3 compares the performance of three types of MCT depending on the type of cooling used.

Table 4.3.3 Comparison between the parameters of different MCT detectors depending on the type of cooling used.

MCT	Spectral response	Responsivity	Single photon detection efficiency	Detectivity	Speed	Operation temperature
Uncooled Thorlabs[1]	2-10.6um	>0,01 A mm/W	0,26% @ peak 4.8um	>2E8 cm Hz^(1/2) W^-1		15 – 30°C
Cooled Daylight Solutions[2]	4-12um	>2500 V/W	* No transimpedance gain given (to transform V/W to A/W)	>2,5E9 cm Hz^(1/2) W^-1	<3ns rise time	-28°C
Cryogenic cooled Light Catcher[3]	2-24um	>1000 V/W	Assuming 10^5 typical value for transimpedance gain <4%	=3.0E10 cm Hz^(1/2) W^-1		-196°C

[1] https://www.thorlabs.com/newgrouppage9.cfm?objectgroup_ID=11689
[2] https://www.daylightsolutions.com/products/amplified-mct/
[3] http://www.light-catcher.com.cn/products.asp?t_classid=111

The specific detection efficiency is not directly given in the examples presented in the table, but it has been estimated for the extreme case of cryogenic cooled detectors by assuming a typical transimpedance gain of 10^5 to transform the responsivity value given in (V/W) into (A/W). Then the quantum efficiency has been calculated as:

$$\eta_{\mathrm{ext}} = \frac{R_{\mathrm{A/W}}\, h\, c}{q\, \lambda}.$$

Nevertheless, the so called "Rule07" gives a more general way to compare the performance between the MCT detectors and the visible range detection options presented in previous tables. The Rule07 predicts the dark current density of MCT detectors depending on their cooling temperature (see Fig. 4.3.1)[63].

[63] Tennant, Journal of ELECTRONIC MATERIALS, Vol. 39, No. 7, (2010)

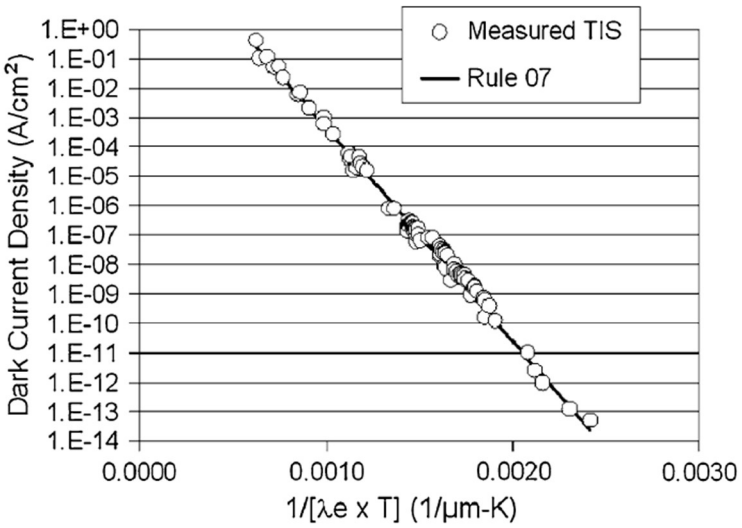

Figure 4.3.1 Rule 07 model compared to measurement results[64]

As a mode of example:

Detection of 10µm wavelength at room temperature would imply to deal with a dark current of ~30A/cm² (or ~2E16 e-/s, assuming a detection area of 0.01mm²). However, if the detector is cooled down to -196°C, the dark current reduces to ~3E-6 A/cm² (or ~2E9 e-/s, assuming a detection area of 0.01mm²).

Using entangled photon sources in an interference-based sensing scheme, MCT detectors could be replaced by a detector in the visible range[65]. Therefore, the dark counts would be significantly lower (in the order of ~10 cps, instead of the ~2E9 e-/s of a cryogenic cooled MCT detector) allowing for better SNR. Moreover, the fact that the VIS detector does not require cryogenic cooling, would reduce the payload in terms of weight, volume, and power consumption. In addition, the complexity of the detector system would be reduced.

In conclusion, two color schemes used for quantum sensing (in particular, interference-based quantum sensing) would offer clear increase in the detection performance in the SWIR – LWIR range as well as reducing the overall instrument payload.

4.4 WP2200 – WP2600: Experimental evaluation of identified challenges

One of the main critical challenges identified for quantum sensing approaches to be feasible for Earth observation applications is the effect that atmospheric turbulences might cause to the performance of such systems. The wavefront distortion expected from atmospheric turbulences might cause the degradation of the spatial correlations required for wide-field and correlation-

[64] Tennant, Journal of ELECTRONIC MATERIALS, Vol. 39, No. 7, (2010)
[65] Kumar et al., Appl. Phys. Lett. 119, 244001 (2021)

based imaging approaches. In addition, wavefront distortions could also lower the visibility and therefore, worsen the signal to noise (SNR) ratio of both, interference- and correlation-based approaches.

These effects are studied experimentally in the lab with a low gain interference-based quantum imaging system[66]. To experimentally simulate atmosphere turbulences, a motorized rotation phaseplate from Lexitek was used. The phaseplates designed and manufactured by Lexitek guarantee a specified Fried parameter (r0) from the user. To estimate a Fried parameter that would map real scenarios into the setup in the lab, the following assumptions are taken:

- Weak turbulences at sea level for visible wavelength (500nm) with r0 = 0.2m[67]. This is a typical value considered in the literature for telescopes located at good observation sites.
- Satellite telescope diameter of 1m
- Idler beam (probing beam) diameter of ~3mm for the lab setup
- Idler beam wavelength of 730nm
- Turbulence volume simulated through a single layer (Fig. 4.4.1)
- Collimated probing beam going through the atmosphere and reflected back (Fig. 4.4.1)

With these considerations, the calculated Fried parameters for different turbulence strengths are summarized in Table 4.4.1. The Fried parameter for weak turbulences is taken from the literature (r0=0.2m). The selection for strong and moderate values is just chosen to be stronger than the typical value for weak turbulences, but not to reach the limit where is no longer valid to model the atmosphere by only one phase screen. Since the Fried parameter of r0=0.2m from the literature is given for a typical 500nm wavelength and for telescopes, we need to scale the Fried parameter to the experimental lab setup that uses 730nm and a beam diameter of ~3mm, following the expression:

$$r_0 = \left[0.42\sec(\zeta)k^2 \int_0^L C_n^2(z)dz\right]^{-3/5},$$

where $k = \frac{2\pi}{\lambda}$, ζ is the zenith angle, and C_n^2 is the atmospheric turbulence strength along the light path z.

The atmospheric turbulence strength C_n^2 is barely wavelength dependent and it is considered constant, and we assume the same path (entire atmospheric profile) as considered in the literature to derive the r0=0.2m value at 500nm. The dependance of the Fried parameter with the wavelength is then the well-known relation $r_0 \sim \lambda^{6/5}$. From this, we calculate the equivalent Fried parameter to be r0=0.31 for the wavelength used in the experimental setup, $\lambda = 730nm$. The ratio between the beam diameter and the Fried parameter needs to stay constant to ensure we

[66] Gilaberte Basset et al., Laser Photon. Rev. **15**, 2000327 (2021)
[67] Andrews and Phillips, "Laser Beam Propagation through Random Media", pg. 608, (2005)

deal with the same turbulence strength. This ratio is then used to calculate the correspondent Fried parameter for the wavelength and the beam diameter (~3mm) used in the experimental setup, giving a value of r0~1mm for weak turbulences (see Table 4.4.1).

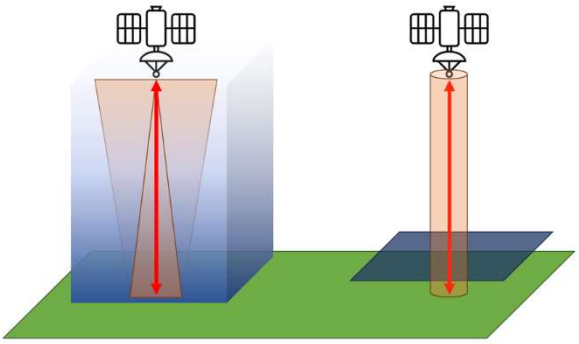

Figure 4.4.1 Sketch of a real down- and uplink scenario (left) and the considered scenario for the experimental measurements (right).

Table 4.4.1 Calculated Fried parameters to scale turbulences reported in the literature to the experimental setup in the lab.

Turbulence strength	**r0 @500nm (m)**	**r0 @730nm (m)**	**$D_{telescope}$ / r0**	**r0 @730nm lab setup equivalent (m)**
strong	0.05	0.08	12.7	2.36E-4
moderate	0.10	0.16	6.4	4.72E-4
weak	0.20	0.31	3.2	9.45E-4

Two phase plates were ordered to Lexitek with r0=0.5mm and r0=1mm to simulate moderate and weak turbulences, respectively.

In addition to the phaseplates, a rotation motor was also purchased that guarantees the simulation of windspeeds up to 50m/s. However, we restrict the analysis of the turbulence effects to windspeeds of 10m/s which corresponds to number 5 in the Beaufort scale and described as "fresh breeze".

Because of the simplified turbulence model considered for the experimental study, the obtained results are only preliminary and further tests in a real environment should be performed. To that end, further tests using a free-space link would need to be considered as next steps to further evaluate the feasibility of quantum sensing techniques (see Sec. 4.6).

The interferometric-based imaging setup used consists on a 405nm CW laser that pumps a 3mm long ppKTP crystal with ~30mW power. The crystal generates pairs of correlated

photons at wavelengths of 730nm (idler) and 910nm (signal). The 730nm light is sent to the object (the one that would be sent to probe "Earth"), and the 910nm is the one detected by the camera. The camera is a back-illuminated scientific CMOS from Photometrics. It should be emphasized that the purpose of this section is not to compare image quality when detecting at 910 nm versus 730 nm, but rather to quantify how turbulence degrades image quality. The chosen detection wavelength is assumed to not influence the degradation behavior. The sketch in Fig. 4.4.2 shows the setup configuration used for ULEO project.

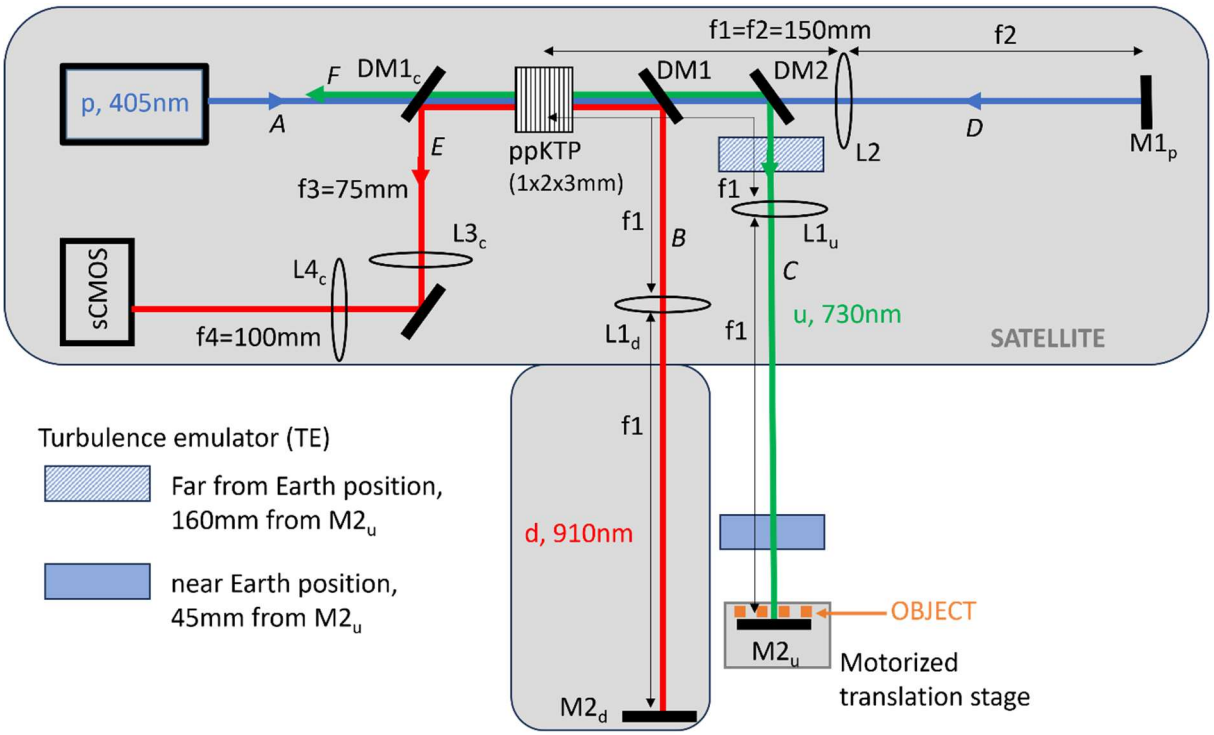

Figure 4.4.2 Sketch of the setup configuration used for ULEO project

The pump beam (A) interacts with the crystal in the forward direction and can generate SPDC beams at 910nm (detected beam,d) and 730nm (undetected beam, u) in the forward direction (B and C, respectively). Beams B and C are reflected back into the crystal with mirrors M2d and M2u. At the crystal, this probability (that detected and undetected beams are generated from the forward interaction of the pump with the crystal) interferes with the probability that detected (E) and undetected (F) beams are generated from the backward interaction of the pump beam (C) with the crystal. This interference appears only if the two possibilities are indistinguishable, by careful alignment of the system. When the idler beams (C and F) are indistinguishable from each other, coherence is induced to the signal (or detected) beam. The lenses L1, L2, L3 and L4 assure that the image of the object is detected at the camera plane. The motorized translation stage was used for the first set of measurements, as it will be introduced later, as part of the image acquisition method. With this setup, the effect of turbulence on the image resolution and SNR was studied when the

turbulence emulator (TE) was placed at two different positions, far from "Earth" at 160mm from M2u and closer to "Earth" at 45mm from M2u. The "far from Earth" position refers to a plane closer to the Fourier plane of an object at Earth (or mirror M2u) than to an image plane or the object itself. In the lab scenario, the 160mm distance from the mirror M2u corresponds to a plane 140mm away from the Fourier plane of the mirror (we use a lens of 150mm focal length). Since after the lens, rays from any point of the mirror emerge parallel, that can be seen as placing the turbulence close to infinity from the mirror/sample/Earth. The "near to Earth" position is when the turbulence plate is close to the mirror (45mm away, that is the closest we could put it due to space limitations). This corresponds to a scenario where the turbulences are close to the Earth surface (or close to the atmospheric layer under study). These two planes could be approximately associated with different effective altitudes of atmospheric turbulence. Obtaining an approximate quantitative mapping between TE position and atmospheric layer would require modeling via ray- transfer matrices, taking into account the illumination geometry - e.g., the distance satellite to- sample distance) and the effective focal length of the optical system.

An image of the setup before introducing the TE, where the beam paths are highlighted for clarity is shown in Fig. 4.4.3.

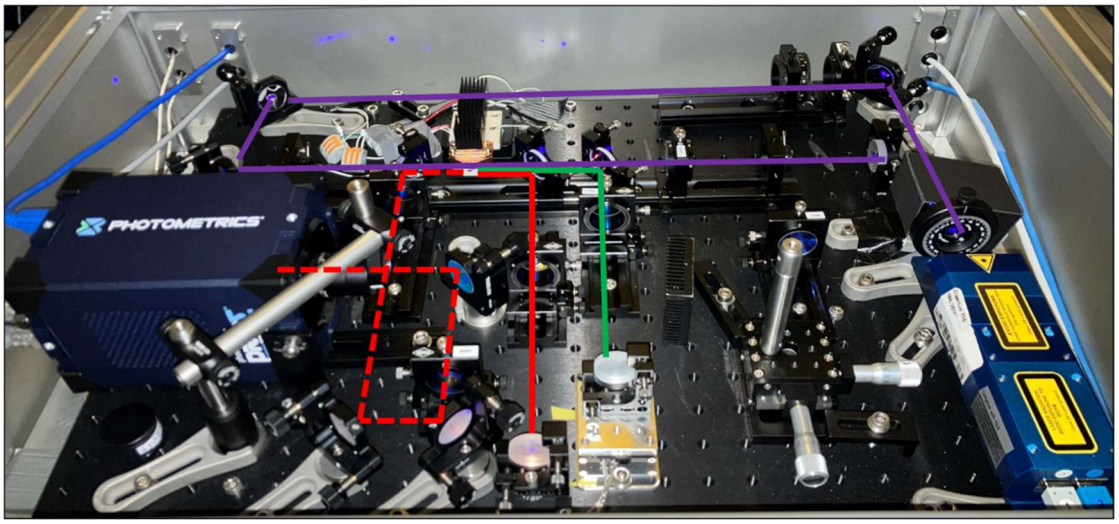

Figure 4.4.3 Experimental setup image. The colored lines highlight the beam paths of the pump (in violet), the idler or probe (in green), and the signal or detected (in red).

Figure 4.4.4 show a closeup of the idler path with the TE at the two different positions, far and close to Earth.

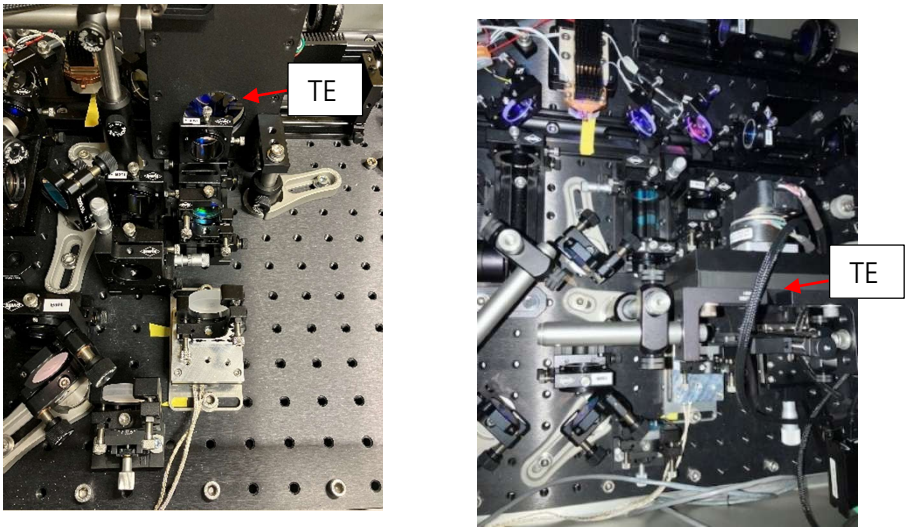

Figure 4.4.4 Close up picture of the idler (or probe) beam at the two different positions, far from Earth (left) and close to Earth (right).

The pump waist at the crystal position is measured to be 165±2µm. The pump waist measured, together with the crystal length and the wavelengths of the generated photons, predict a spatial resolution of 150.5µm [68]. The signal and idler beam diameter are also measured, as it is a relevant value in order to calculate the Fried parameter required for the phaseplate that simulates the atmospheric turbulence in the lab. The idler, or probe, beam diameter is 2820±85µm.

The idler photon flux that undergoes the turbulence path is measured to be 1.57E6 photons/(s*mW*nm) for this specific source. Higher photon flux are reported when choosing different sources, e.g. for ppKTP waveguides instead of the bulk crystal in use here, a flux of 2.5E8 photons/(s*mW*nm) is reported[69]. This fluxes are not enough for Earth observation applications, but the focus of this experimental study is about the effect of the turbulences on the imaging system. Nevertheless, higher photon fluxes are achieved when operating this quantum sensing techniques in a high gain regime, by pumping the nonlinear crystal with high power lasers or by seeding the nonlinear process. A more detailed study on the returned signal for low and high gain regimes is presented as the results of WP3000 of this project in Section 4.5.

To be able to compare the effects of the turbulence on the imaging system, the system performance is first analysed without turbulence in terms of visibility of the interference (which relates to the SNR) and spatial resolution. At this point is important to mention the image acquisition method used for these initial tests is the classical holography technique

[68] Gilaberte Basset et al., Proc. SPIE 13392, Quantum Sensing, Imaging, and Precision Metrology III, 133920U (19 March 2025) https://doi.org/10.1117/12.3037258
[69] J. Chen, et al., Opt. Express **17**, 6727–6740 (2009)

called digital phase-shifting holography (DPSH), which allows to simultaneously obtain the transmission and the phase of the probed object by taking a minimum of three images at different interferometric phases[70].

Visibility achieved in first alignment stages was of only 36% because of an unwanted leakage of pump wavelength into the signal and idler arms due to not optimal performance of the dichroic mirrors used. This leakage was later on corrected by adding long pass filters on both arms and visibilities of ~70% achieved. However, first measurements on spatial resolution resulted in a measured resolution of 160±10µm in agreement with the predicted resolution (150.5µm). For this measurement, the transmission image of a sharp edge was calculated from a set of images 6 images taken at 6 different interferometric phases with 300ms integration time each. Next image is a transmission image that resulted from this measurement, where it can be seen that the sharp edge is blocking the right side of the beam and therefore, transmission at the covered area drops to zero while transmission on the non-blocked area is maximum (and equal to the visibility). The resolution value is the average of the resolution calculated from 10 transmission images constructed from a DPSH algorithm.

A region at the centre of the beam (marked in dashed red lines in Fig. 4.4.5) is evaluated to extract the normalized edge profile (blue line in Fig. 4.4.5). The resolution is calculated as the spread of the line spread function (LSF), which for our case corresponds to the point spread function (PSF), of that edge when the intensity falls to 1/e of the maximum intensity.

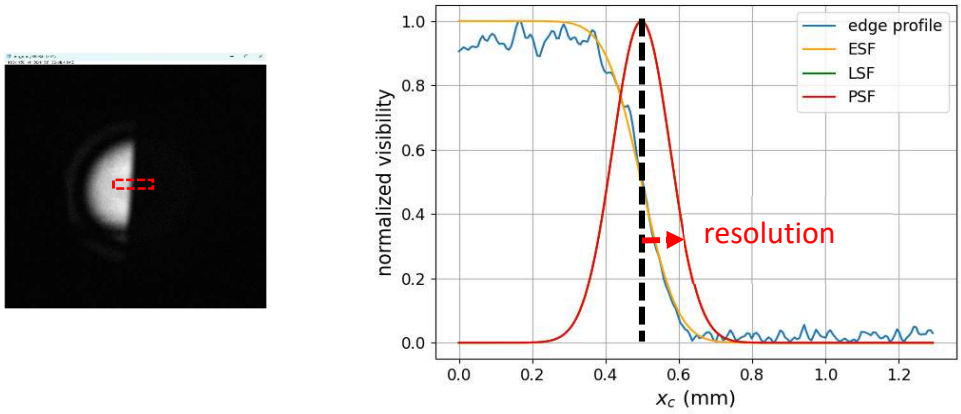

Figure 4.4.5 Example of the evaluation of the image resolution from an image of a sharp edge.

The SNR is measured to be 27.0±0.4. This value is the average of the SNR calculated for the 10 images evaluated. The signal level is considered as the maximum intensity of the not normalized edge profile, while the noise level is the averaged intensity of the edge profile curve after the point where the intensity decays to $1/e^2$.

Next step is to evaluate the performance of the system with the rotating phaseplate at a position that simulates turbulences far from Earth, for different rotation speeds. Weak turbulences are

[70] Töpfer, Gilaberte Basset et al., Sci. Adv. **8**, eabl4301 (2022)

analysed. After re-adjusting the interferometer arm length to compensate for the optical path length introduced by the phaseplate, same analysis on visibility and resolution is performed.

However, it soon became clear that the image acquisition technique is not suited for scenarios with turbulence because the DPSH technique requires the acquisition of a reference image (when no object is present) together with the object image. Since the turbulence fluctuation is too fast compared to the image acquisition time, the resulting transmission image has no useful information. The images shown in Fig. 4.4.6 are an example of transmission images when weak turbulence and windspeeds of 1m/s are present from which is clear that no clear information of the presence of an edge is collected.

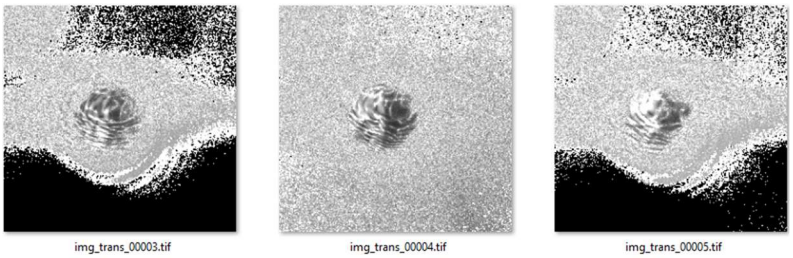

Figure 4.4.6 Examples of transmission images when weak turbulence and windspeeds of 1m/s are present

Although from the visibility images (Fig. 4.4.7) it is still possible to evaluate the edge resolution, it would still be not longer possible to separate transmission from phase information of the object.

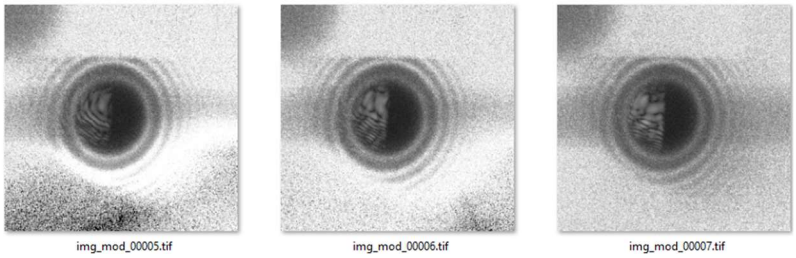

Figure 4.4.7 Examples of visibility images when weak turbulence and windspeeds of 1m/s are present

Therefore, we changed the image processing technique to off-axis holography instead of the DPSH. Off-axis holography allows to gather transmission and phase information without the need of the reference image[71]. In addition, this method offers a better stability against changes in the laboratory conditions such as temperature fluctuations and mechanical vibrations. Therefore, it enables the study of dynamic behavior within a shorter time window compared to DPSH. All these features make off-axis technique a more suitable approach for Earth observation applications.

[71] León-Torres et al., Opt. Express **32**, 35449-35461 (2024)

The off-axis technique relies on introducing an angle between the forward and backward generated beams. That causes the +1, direct term, and -1 diffraction terms to separate in the Fourier space. The larger the introduced angle, the more separated are the first order diffraction terms from the direct term and the easier they can be isolated from the noise encoded in the direct term. However, this angle introduces some distinguishability into the system which causes the interference visibility to decrease. Therefore, a trade-off has to be considered between visibility (or the signal) and the reduction of noise. From either of the two first diffraction order terms, the phase and transmission of the object can be retrieved. From our previous work on the robustness to misalignments of this interference-based schemes[72], a tilt in the signal mirror (the one staying at the satellite) is the desired one to introduce the required angle for off-axis holography to work while maintaining the highest visibility of the interferometer.
Figure 4.4.8 show an example of the RAW intensity images collected with the camera when an object is blocking the right side of the beam, and when the object would cover the entire beam.

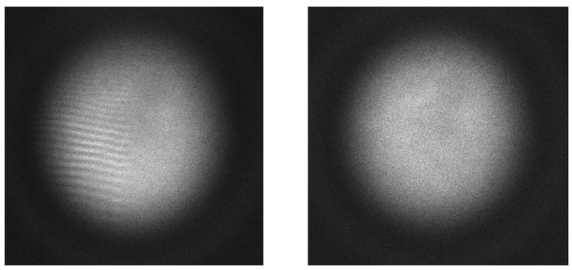

Figure 4.4.8 RAW intensity image when an object is blocking the right side of the beam (left), and when the object would cover the entire beam (right).

The right image in Fig. 4.4.8 is taken as the reference beam for the off-axis holography and is then subtracted from the object image to enhance the visibility of the fringes[73]. This is done for each measurement. Figure 4.4.9 show an example of the RAW image and the result image when subtracting the reference image.

[72] Gilaberte Basset et al., Laser Photon. Rev. **15**, 2000327 (2021)
[73] Pearce et al., Sci. Rep. **14**, 16008 (2024)

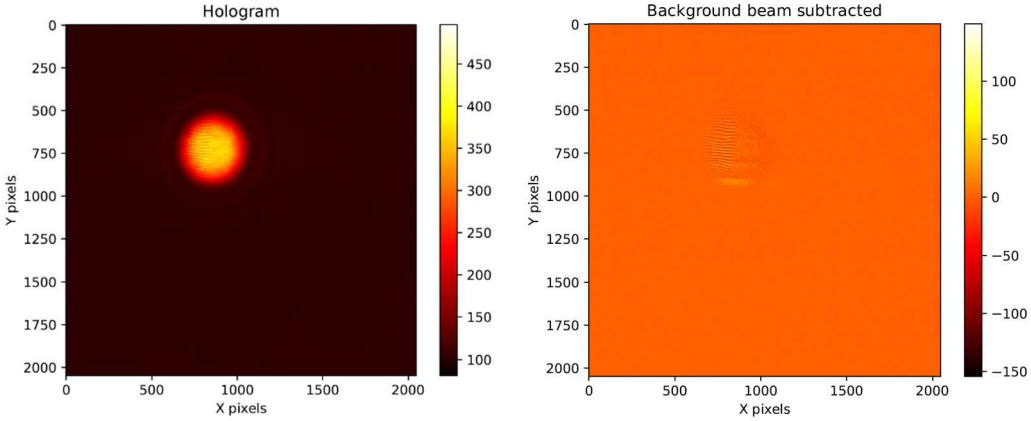

Figure 4.4.9 Example of the RAW image (left) and the enhanced image when subtracting the reference image (right)

From this reference-subtracted image (or hologram), the Off-axis reconstruction process is summarized in the sketch from Fig. 4.4.10[74].

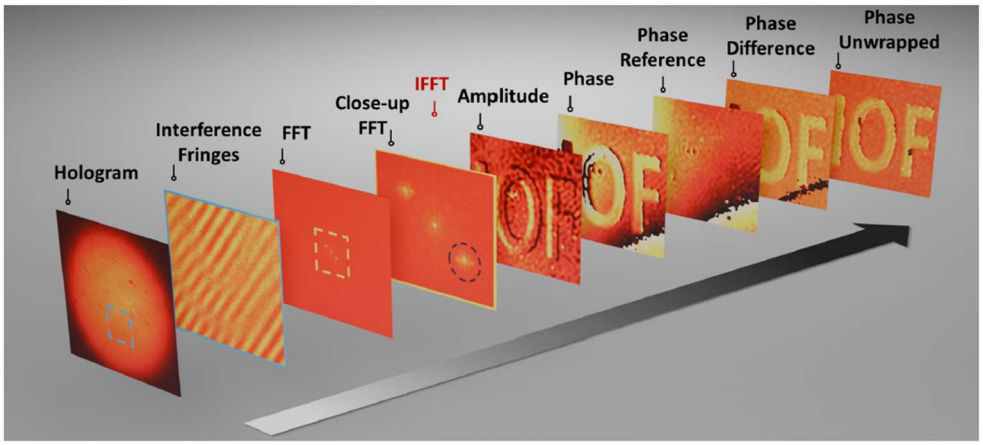

Figure 4.4.10 Sketch of the Off-axis reconstruction process

Amplitude images are in fact a spatial map of the transmission of the object under study. Since the edge object used for the resolution analysis is a transmission object, amplitude images were the ones analyzed to obtain the resolution and SNR of the images of the edge following the same process used to analyze the images without turbulence. In this case, 20 amplitude images were considered to calculate an average value for the resolution and SNR. The goal is to have enough images representative of different phases introduced by the turbulence. The image acquisition time is 300ms and the windspeeds introduced correspond to a range between 0.03 and 0.3 revolutions/s of the phaseplate. For the slower windspeed, that means that one image contains the integrated phase changes over ~3° of a rotation. One would need 110 images to cover one

[74] León-Torres et al., Opt. Express **32**, 35449-35461 (2024)

rotation. For the highest windspeed tested (10m/s), 20 images cover more than one revolution of the phaseplate. With the photon flux from the source we use, lower acquisition times (<100ms) are available but at the expense of lower SNR. To achieve even shorter acquisition times without compromising the SNR, higher photon flux generated at the crystal would be necessary. That is typically achieved with higher pump powers. Smaller pump waists and longer crystal lengths would also result in more photon flux, but at the expense of decreasing spatial correlations strength.

The effect of weak turbulences when increasing the windspeed on the image resolution is tested in the lab, and the results obtained indicate that there is no degradation of the image resolution due to atmosphere turbulence (Fig. 4.4.11). That means that the spatial correlations between the signal and idler photons seem to be robust to atmospheric turbulence.

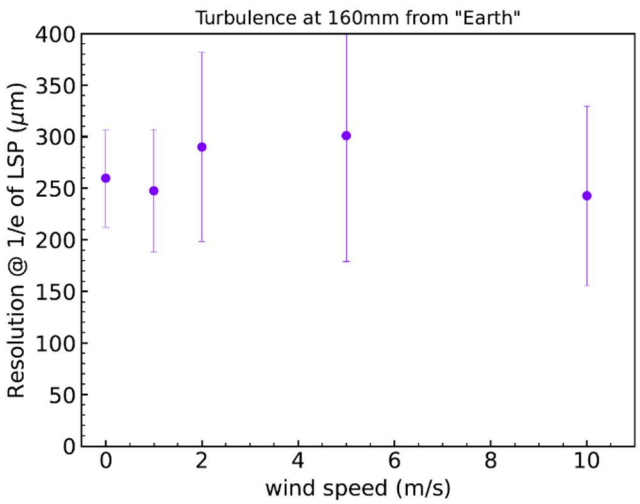

Figure 4.4.11 Resolution measured as the spread at 1/e of the LSF for different windspeeds when turbulence emulator is placed at the "far from Earth" position.

This is an important first result since it allows to consider wide-field quantum imaging approaches as possible tools for Earth observation applications, contrary to initial expectations.

On the other hand, turbulences do show an effect on the image SNR which slightly decreases with increasing windspeeds (Fig. 4.4.12).

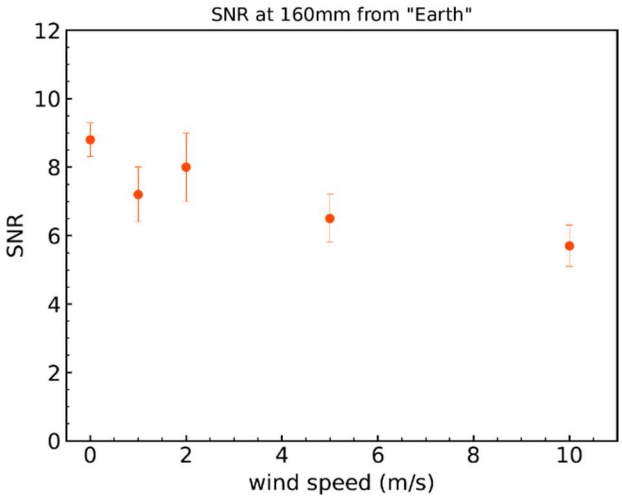

Figure 4.4.12 SNR measured for different windspeeds when turbulence emulator is placed at the "far from Earth" position.

The overall SNR is expected to be higher when carefully post-processing the data for optimal SNR.

The same analysis is also performed to simulate turbulences closer to Earth, in our setup that means that the turbulence emulator is placed at 45mm from $M2_u$. However, due to space restrictions, the object is ~5mm away from $M2_u$ surface. Therefore, there is a ~5mm difference in the object position when analyzed with far and near to "Earth" turbulences. The results show the same promising effect of turbulences on both, image resolution and SNR, as when simulating far from Earth turbulences.

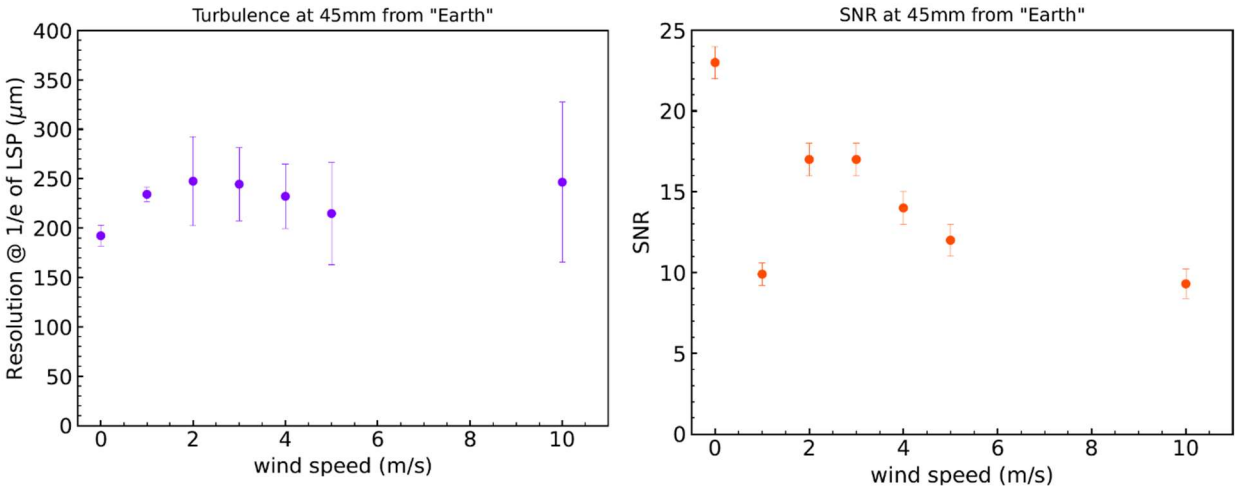

Figure 4.4.13 Resolution measured as the spread at 1/e of the LSF (left) and SNR (right) when turbulence emulator is placed at the "near to Earth" position.

The smaller error bars and higher SNR are result of the proper reference subtraction on the edge image. The reference image for this last results is taken from the idler (or probing) beam, while for the previous results was wrongly taken from the signal beam. Due to time constraints, the measurements for "far from Earth" turbulences could not be repeated with the correct reference beam.

The SNR drop at 1m/s in Fig. 4.4.13 is caused by an analysis artifact and not by a system sensitivity at that windspeed. The reason for that is that the data for which an edge function can not be fitted (see Fig. 4.4.16), is excluded for the analysis. However, for that particular measurement, two images for which the fit could be found, the SNR is much lower than the rest, thus decreasing the SNR of the whole set.

In addition, when the rotating phaseplate is close to the mirror $M2_u$ (and to the edge object) the motor vibrations have a clear effect on the worsening of the image resolution and SNR. To quantify this effect, the resolution and SNR values of images taken with the rotating motor off and on (rotating at 1m/s) but without phaseplate (no turbulences) are compared in the Table 4.4.2. These results show a clear degradation in the SNR solely due to motor operation.

Table 4.4.2 Resolution and SNR values when no phaseplate is mounted in the rotation motor to quantify the degradation of the image solely coming from the motor operation.

	Resolution (µm)	**SNR**
No motor	213±12	27±1
Motor rotating @1m/s without phaseplate	227±38	14.9±0.9

Therefore, the results simulating the effect on image resolution and SNR for turbulences close to Earth (shown in Fig. 4.4.13) not only show the effect of turbulences but also include the effect of the vibrations caused by the rotation motor affecting both, the interferometer stability and the object stillness, which may be considered as a simulated atmospheric piston.

Although these are very promising initial results, further studies would be needed to analyze the behavior not only under stronger turbulences, but also to consider the effect of different wind directions and a volume of turbulences instead of approximating that to a single layer. Some of these studies might be easier to be performed directly in free-space links rather than in a lab environment. Our group in IOF has this infrastructure available and already in use for quantum communication measurements. Therefore, it could be feasible and relevant to perform tests on the effect of turbulence in a real turbulence environment.

Moreover, further considerations would have to be taken to maybe optimize the analysis process. As mentioned, 20 amplitude images are taken to calculate the average resolution and SNR

presented. In addition, some areas of the hologram do not present interference fringes. As a consequence, for these regions, the intensity of the amplitude image decreases and even drops to zero for some regions as shown below (lower row in Fig. 4.4.14). For comparison, the upper row in Fig. 4.4.14 shows the hologram and corresponding amplitude image when no phaseplate is present.

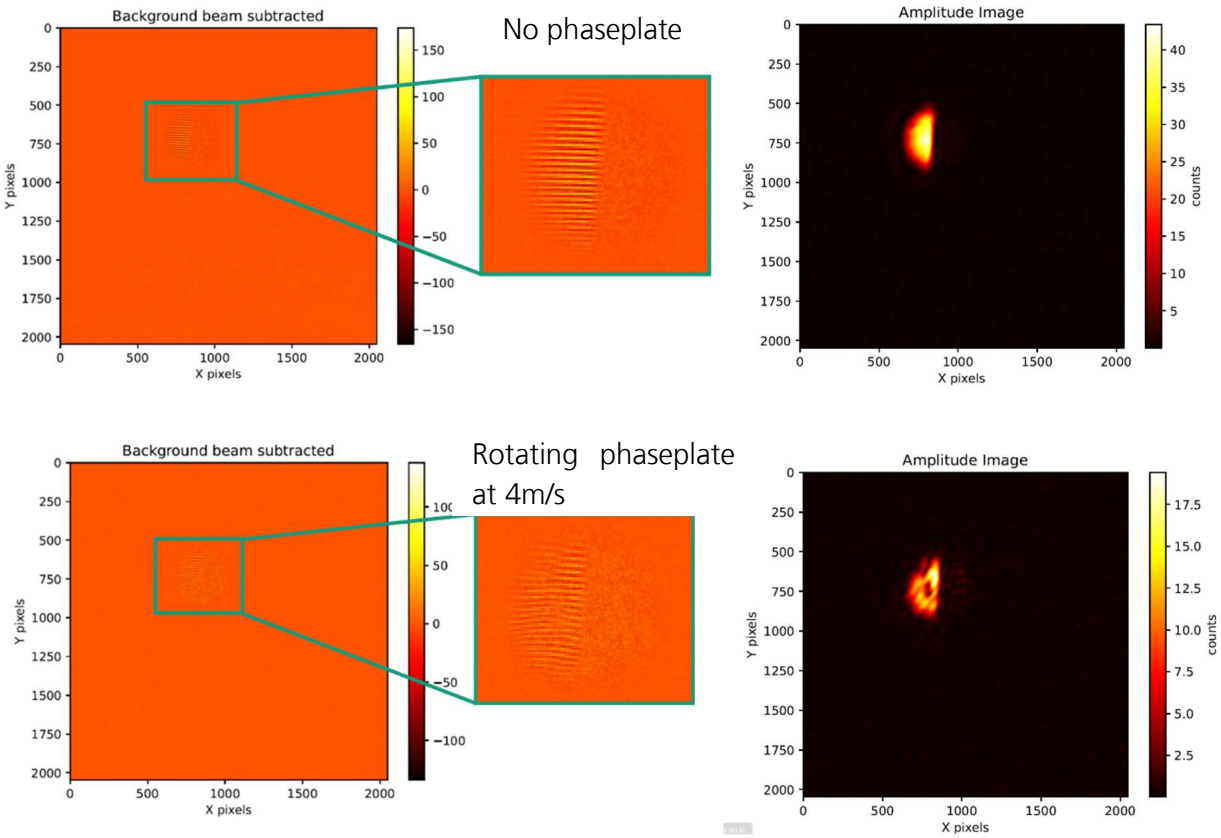

Figure 4.4.14 Hologram and corresponding amplitude image when no turbulence emulator (TE) is present (upper row). The lower row shows an example of the recorded images when the TE is present, which show some areas without interference.

Different possible causes for the decrease of the interference visibility observed in some areas are considered and analysed.

- Alignment issue: discarded, since this effect is not present in the images without turbulence
- Height difference imprinted in the phaseplate is larger than the coherence length: discarded after Lexitek confirmation on the maximum optical path length introduced is 6.5µm, which considering the double pass of the light through the phaseplate means that a maximum of 13µm are introduced by the phaseplate engravings. This is still well inside the coherence length (~0.42mm).

- Manufacturing and mounting stress inducing birefringence in the phaseplate which could cause polarization rotation effects: discarded after measuring the phaseplate with a polarimeter. The visibility decrease caused by polarization effects would be between 0.01 – 0.001% which does not correspond to the effects observed.
- The phaseplate has not an homogeneous transmission: probable cause. A classical image with 730nm was taken with the same imaging configuration used for the study. That is achieved by blocking the signal and the pump paths in the interferometer, thus just letting the forward idler beam to be present in the system, and exchanging the filters in front of the camera to let pass the idler beam instead of the signal. The raw images recorded with the phaseplate at a position far from "Earth" and close to "Earth" (see Fig. 4.4.15) revealed a transmission pattern on the phaseplate.

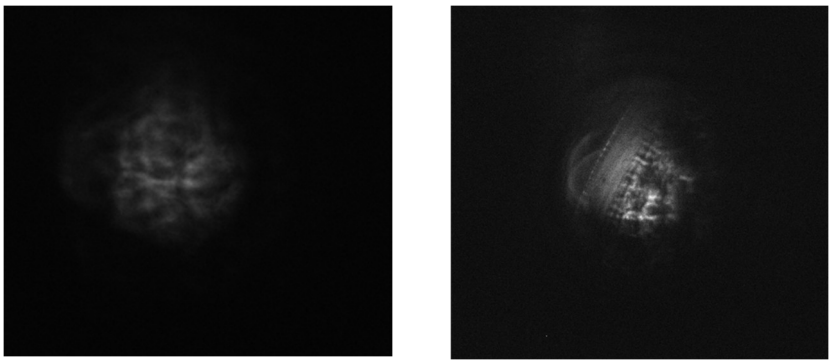

Figure 4.4.15 RAW images recorded with the phaseplate at a position far from "Earth" (left) and close to "Earth" (right)

The process followed to analyze the image resolution and SNR could probably also be improved. For each of the 20 images analyzed, the brightest area of 20 pixels height along the edge is analysed and an edge spread function is fitted to the edge profile (see Fig. 4.4.16).

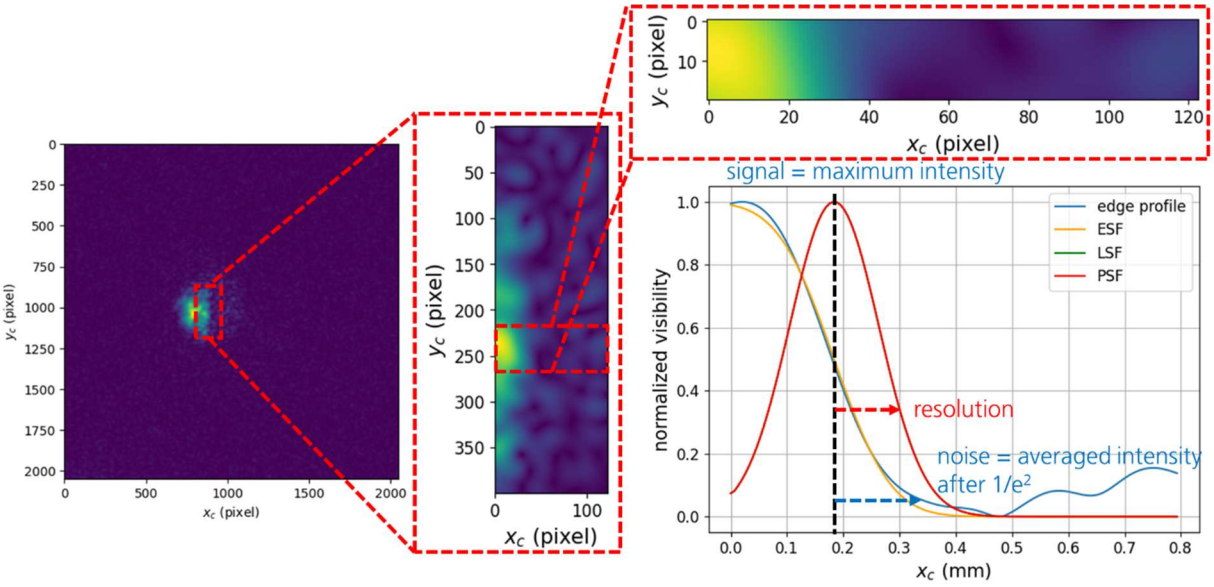

Figure 4.4.16 Example of the process followed to analyze the image resolution and SNR

Sometimes, this fitting fails because of either a too noisy image or a too inhomogeneous signal due to the visibility decrease effects just discussed. These images, for which the fitting fails, are not considered for the calculation of the mean values presented. Although the noise coming from decoherence effects affects the image and the ability to analyse the edge function, as long as one can still measure the sharpness of the edge, one has a direct access to the loss of correlation strength (or image resolution). The decoherence (understood as the intensity variation per pixel) would just affect the SNR.

In addition, the fact that the decoherence caused by turbulences introduce random intensity variation per pixel in the processed images shows that a more careful study on different image reconstruction algorithms would be necessary in order to be able to distinguish between turbulence effects and object features.

Moreover, improved algorithms for phase detection or noise reduction could be researched in order to optimize the information extracted from the obtained images.

In conclusion, although further studies would be necessary to assess the robustness of interference-based quantum imaging to atmospheric turbulence in more detail, the initial results performed in the framework of ULEO demonstrate for first time that spatial correlations seem to not degrade under the effect of weak turbulences.

4.5 WP3200 – WP3400: Evaluation of identified challenges with simulation

One way to evaluate the performance of a satellite-based quantum imaging system in Low Earth Orbit (LEO) is to leverage the established link loss budgets derived from LEO Quantum Key

Distribution (QKD) experiments. Link loss budgets for QKD consider critical factors such as atmospheric attenuation, beam divergence, pointing errors, and optical system efficiencies. These same considerations are directly relevant to a quantum imaging setup, as both systems often use similar optical hardware and must contend with many of the same propagation challenges. By drawing on the heritage of existing QKD link budgets, developers can save time and resources in estimating the required laser power, telescope apertures, and overall design parameters for a proposed quantum imaging mission.

We employing a modeling of Loss budget in a satellite for quantum Key distribution (QKD) in a dual link configuration as shown in figure 4.5.1, and more detailed discussed in[75] . We adapted the existing QKD code to evaluate the feasibility of a Quantum imaging system for Earth observation missions in LEO orbit. We start by restructuring the former approach including the two different techniques from quantum imaging as previously described. Correlation – and interference -based sensing.

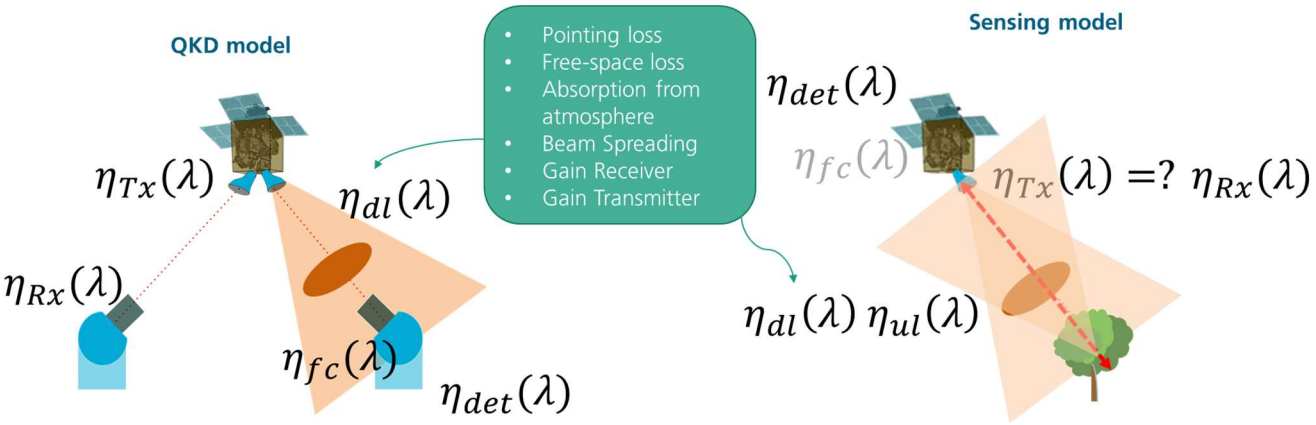

Figure 4.5.1. left: QKD dual link loss model. Right: QSensing model for elastic backscattering

Following the approach in Kržič et al. we select the parameters along the communication channel which affect the performance of the QKD protocol. To be more clear, we divided the communication pipeline into three main parts for a more comprehensive analysis as detailed in the Table 4.5.1:

A) Inter-satellite parameters: This compile mainly the losses from the Entangled Photon source (EPS) up to the emitter telescopes.

B) Free-space link parameters: free-space link budget between the satellite and the optical ground receiver.

[75] *Andrej Krzic et al. Proc. SPIE 12777, 1277726 (12 July 2023); doi: 10.1117/12.2689971*

C) Internal Optical Ground Station parameters: This section considers the losses induced in the reception optics and the detection electronics of the OGS.

Table 4.5.1: Usual Link budget for QKD Model in dual link configuration

Main Section	Parameters	Value
A	EPS intrinsic generation rate	Depending on mission requirements
	EPS intrinsic heralding	0,47 (for 1550 nm), 0,80 (for 810 nm)
	QKD baseline error rate	0,02
	Transmitter aperture diameter (m)	Depending on the mission scenario
	Transmitter pointing jitter (s)	1,00E-06
	Transmitter optics transmittance	0,75 (wavelength dependent)
B	Zenith angle Alice (rad)	Depending on mission requirements
	Zenith angle Bob (rad)	Depending on receiver location
	Satellite distance Alice (Km)	Depending on mission requirements
	Satellite distance Bob (Km)	Depending on mission requirements
	OGS altitude Alice	187,0
	OGS altitude Bob	579,0
	Atmospheric transmittance at zenith	0,783
	Background Solar spectral radiance [W/sr/m^3]	1 (At night), 1,00E+06 (Day light with moderated intensity)
	Alice link loss	Depending on satellite distance
	Bob link loss	Depending on satellite distance
C	Detection time jitter per site (s)	400 ps (SPADs for 810 nm)
	Coincidence window	5 * Detector jitter
	Dark count rate per detector	1,00 cps
	Detector efficiency (%)	> 80,00
	Detector dead time (s)	2,00E-10
	Error correction efficiency	1,22
	Coupling	SMF (day light), MMF (night-time)
	MMF core diameter (m)	30,00E-06
	MMF numerical aperture	0,275
	Receiver optics transmittance	0,75 (for 1550 nm), 0,60 (for 810 nm)
	Receiver AO correction level	Tip-tilt (MMF coupling), full (SMF coupling)
	Receiver aperture diameter (m)	0,8
	Receiver obscuration diameter	0,328

Receiver spectral filter bandwidth (m)	3,00E-09

The parameters above are the minimum necessary to achieve the identification of the optimal values for asymptotic Secure Key Rate (SKR) and Intrinsic Brightness of the Entangled Photon Source (EPS) as optimal threshold values for the mission.

In a quantum imaging context, high-fidelity photon detection is essential, and the knowledge gained from QKD—where low signal-to-noise ratios must be carefully managed—can inform hardware improvements and system-level tradeoffs. Ultimately, this overlap allows for a systematic approach to designing robust quantum imaging missions in LEO. By building on proven QKD solutions, it becomes more feasible to assess technical requirements, cost-effectiveness, and overall feasibility, thereby accelerating progress toward real-world quantum imaging applications in space.

To achieve this approach we use the described code for QKD applications and modify it to extract the modules requires for the Earth observation scenario. As has been discussed over this report the Quantum imaging techniques here described are divided in interference and correlation based techniques. In the same way, we organize the code in modules that can be use in each of the cases. However, the common root for both of the scenarios is the loss budget of the traveling photons considering the path from the quantum source towards the object and the return way. In the follow we explain in detail the assumptions and model use to achieve this estimations as close as possible to a real scenario.

4.5.1 Returned photons calculation

To compare with the classical case of a backscatter lidar we estimate the total losses considering a simple scenario:

1. we have single photons traveling toward the object to detect
2. At the photon return we have at least one entangled photon to evaluate the correlations or herald the photon arrival.

Under the first consideration the single count of arrival photons (S_{det}^{i}) is described by[76] :

$$S_{\mathrm{det}}^{\mathrm{i}} = S_{\mathrm{true}}^{\mathrm{i}} + S_{\mathrm{back}}^{\mathrm{i}} + S_{\mathrm{dark}}^{\mathrm{i}} \quad (1)$$

Where the S_{back}^{i} and S_{dark}^{i} represents the counts due to the back radiance light and dark counts respectively. The back radiance light is originated external light sources and depends mostly on the connection way to the detector which could be multimode or single mode if the system employs fiber to arrive to the detection system.

[76] *Andrej Krzic et al. Proc. SPIE 12777, 1277726 (12 July 2023); doi: 10.1117/12.2689971*

The S^i_{true} contains the information about the way follow by the traveling photon in the total optical path[77]

$$S^{\mathrm{i}}_{\mathrm{true}} = \eta^{\mathrm{i}} G \tag{2}$$

Where G is the total amount of photons produced by the quantum source in one second, for the bipartite entangled case is the Brightness, and η^i is the total losses over the quantum channel described by:

$$\eta^{\mathrm{i}} = \eta^{\mathrm{i}}_{\mathrm{EPS}} \eta^{\mathrm{i}}_{\mathrm{Tx}} \eta^{\mathrm{i}}_{\mathrm{DL}} \eta^{\mathrm{i}}_{\mathrm{Rx}} \eta^{\mathrm{i}}_{\mathrm{FC}} \eta^{\mathrm{i}}_{\mathrm{det}} , \tag{3}$$

Here the η^i_{EPS} is the intrinsic heralding in the case of an entangled Photon source defines the contributions from signals and idler right after the crystal in an SPDC case. The η^i_{Tx} is the transmittance of the optics from the transmitter system, η^i_{RX} is the transmittance Optics in the receiver system, η^i_{FC} is the losses due to the fiber coupling, η^i_{det} the detector efficiency, and the η^i_{DL} is the losses in the optical link. This last factor describes the main path followed by the traveling photon including the environmental interactions like the atmosphere absorptions in a satellite case. The conception of this model is mainly heritage from the laser communication, then here we include the transmitter Gain (G^i_{Tx}), free space loss (L^i_{FS}), pointing loss (L^i_P), beam spreading loss (L^i_{BS}), receiver gain (G^i_{Rx}), and atmospheric loss ($\mathrm{L}^{\mathrm{i}}_{\mathrm{atm}}$)[78] .

$$\eta^{\mathrm{i}}_{\mathrm{DL}} = G^{\mathrm{i}}_{\mathrm{Tx}} L^{\mathrm{i}}_{\mathrm{p}} L^{\mathrm{i}}_{\mathrm{FS}} L^{\mathrm{i}}_{\mathrm{atm}} L^{\mathrm{i}}_{\mathrm{BS}} G^{\mathrm{i}}_{\mathrm{Rx}} , \tag{4}$$

In a back scatter LIDAR system, the returned signal depends on range resolution (Δz) and the backscattering probability. In the current case considering long distance traveling (satellite LEO case) the beam spreading makes possible to consider as an initial approach the back scattering probability as in the classical case

$$\beta_{total}(z,\lambda) = \beta_{Rayleigh}(z,\lambda) + \beta_{Mie}(z,\lambda) \tag{5}$$

In our current approach we calculate the backscatter coefficient for aerosol from the spherical particle approximation by employing Mie Theory which provides an exact analytical solution for the scattering of electromagnetic radiation by homogeneous spherical particles. While real aerosols aren't always perfectly spherical (e.g., dust), Mie theory is a fundamental tool and often a good approximation, especially for aged or coated particles. The backscatter coefficient It's

[77] *Neumann, Sebastian Philipp et al, Phys. Rev. A* ***104****, 022406 (2021)*

[78] *Larry C. Andrews, Ronald L. Phillips, Laser Beam Propagation through Random Media, Second Edition, https://doi.org/10.1117/3.626196 (2005)*

fundamentally linked to the size, shape, concentration, and composition (refractive index) of the aerosols, as well as the wavelength (λ) of the incident light. We use the PyMiescatt package which requires the wavelength and the **Complex Refractive Index of the Aerosol Material (m=n+ik)** which describes how light interacts with the material itself.

- 'n' is the real part (related to the phase velocity of light in the material).
- 'k' is the imaginary part (related to absorption).

Then after calculate the backscattering properties of only one spherical aerosol we require the **Particle Size Distribution (PSD)**, often denoted as n(r), describes the number concentration of particles per unit volume as a function of particle radius r. As initial approach we use the log-normal distributions. The shape and parameters (e.g., mode radius, standard deviation) of the PSD are crucial and vary significantly between different aerosol types (e.g., fine mode pollution vs. coarse mode dust).

In this calculation we use the following procedure:

- **Single Particle Properties:** Mie codes first calculate the scattering properties for a *single* spherical particle of a given radius r and refractive index m at wavelength λ. Key outputs are:
    - Scattering cross-section ($\sigma_{sca}(r,m,\lambda)$)
    - Absorption cross-section ($\sigma_{abs}(r,m,\lambda)$)
    - Extinction cross-section ($\sigma_{ext}=\sigma_{sca}+\sigma_{abs}$)
    - Phase function ($P(\theta,r,m,\lambda)$), which describes the angular distribution of scattered light. It's normalized such that its integral over 4π steradians is 4π.

Then, once we have the properties of individual aerosols, we integrate the single-particle properties over the particle size distribution n(r):

- Volume Scattering Coefficient: $\sigma_{sca}(\lambda)=\int \sigma_{sca}(r,m,\lambda)n(r)dr$
- Volume Absorption Coefficient: $\sigma_{abs}(\lambda)=\int \sigma_{abs}(r,m,\lambda)n(r)dr$
- Volume Extinction Coefficient: $\sigma_{ext}(\lambda)=\sigma_{sca}(\lambda)+\sigma_{abs}(\lambda)$
- Volume Phase Function: $P(\theta,\lambda)=1/\sigma_{sca}(\lambda)\int P(\theta,r,m,\lambda)\sigma_{sca}(r,m,\lambda)n(r)dr$

Finally, The volume backscatter coefficient $\beta(\lambda)$ is calculated from the volume scattering coefficient and the volume phase function evaluated at $\theta=180^\circ$:

$\beta(\lambda)=\sigma_{sca}(\lambda)4\pi P(180^\circ,\lambda)$

the value $P(180^\circ,\lambda)$ is the backscatter phase function value calculated in the previous step.

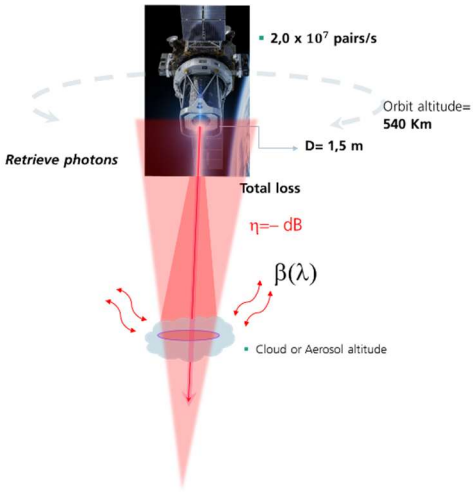

Figure 4.5.2. Low Gain Scenario for an Elastic LiDAR with an imaging setup on Board

As shown in figure 4.5.2, the nature of the problem requires a modification in our current considerations in the eq.4, to include the uplink expressions to achieve a realistic loss budget. In this sense the eq. 4 becomes

$$\eta_{total} = G_{\{Tx\}} L_{\{FS\}} G_{\{Rx\}} L_{atm}^2 L_{BSD} L_{BSU} \qquad (6)$$

Where $L_{BSD} = \frac{1}{\sqrt{(1+T_D)}}$ with $T_D = 4.35\Lambda^{5/6} k^{7/6} (H-h_0)^{5/6}\, csc\, \alpha^{11/6} \int C_n^2(h) \left(\frac{h-h_0}{H-h_0}\right)^{5/3} dh$ estimates the beam spreading in downlink configuration due to the turbulences in the atmosphere. And $L_{BSU} = \frac{1}{\sqrt{(1+T_U)}}$ with $T_U = 4.35\Lambda^{5/6} k^{7/6} (H-h_0)^{5/6}\, csc\, \alpha^{11/6} \int C_n^2(h) \left(1 - \frac{h-h_0}{H-h_0}\right)^{5/3} dh$ is the beam spreading due to the turbulences in uplink configuration.

Then finally, an expression to give information of the retrieve amount of photons will be

$$S_{true}^i(z,\lambda) = \eta(z,\lambda)^i \cdot G \cdot \Delta z \quad (7)$$

Where $\eta(z,\lambda)^i = \eta^i \cdot \beta_{total}(z,\lambda) \cdot {L_{atm}^i}^2$ contains the probability to retrieve signal from a backscatter process. Once we calculate the amount of retrieve photons each technique requires calculate different figures of merit to evaluate the feasibility as follow.

Due to the high losses that involve the satellite implementation of this quantum imaging techniques, we need to consider two regimes to work with. The first, so call Low gain (LG) refers to the average amount of photons (Brightness) produced in a laboratory setup of the order of ***~10⁷ photon pairs/s*** [79], *and the second High gain (HG) regime of the order of* ***~10¹² photon pairs/s*** [80]***.***

[79] *Emma Brambila,et al.," Opt. Express **31**, 16107-16117 (2023)*

[80] *Hashimoto, K. et al., Commun Phys **7**, 217 (2024)*

4.5.2 Interference -based algorithm

As we discussed, the general block of calculation (blue part in figure 4.5.3) is the returned photons from the Aerosol or surface interaction. With this information, the interference-based method could be evaluated considering the expected ***visibility*** of the interference fringes at the satellite interferometer. At this point, it is important to mention that the effect of the losses in the probe beam on the visibility is less sever in the high gain (HG) regime than in a low gain (LG) scenario. That can be concluded from the expression of the visibility for low- (V_{LG}) [81] and high-gain (V_{HG}) [80] regimes:

$$V_{LG} = \frac{2t_p t_d t_u}{(t_d^2 + t_p^2)} \qquad (8)$$

$$V_{HG} = \frac{2t_d t_u}{(t_d^2 + t_u^2)} \qquad (9)$$

where $t_{p,} t_d, t_u$ are the transmission coefficients of the pump, detected, and undetected beam paths respectively. For the expression of the visibility in a high gain scenario, it is considered $t_p = 1$.

For instance, a decrease of 10% in the intensity of the returned signal implies a 10% decrease in visibility for a low gain scenario (as it exists a linear relation between the transmission of the undetected beam path and the visibility). For a high gain scenario, this 10% decrease in intensity of returned signal implies only a 1% decrease in visibility. In this case, there is not a linear relation between the transmission of the undetected beam path and the visibility, e.g. a 50% decrease would translate in 20% loss in visibility. These values are evaluated assuming $t_p = 1$ and $t_d = 1$ to keep the comparison simple. Nevertheless, it is worth noting that for scenarios where high losses are present, the visibility can be improved by optimizing the transmission values for the pump and detected beam paths as well as the gain of the source [82,83].

Therefore, working in the high gain scenario not only assures more returned signal but also a higher resilience of the visibility against losses.

[81] *Gilaberte Basset et al., Laser Photonics Rev.* ***15****, 6 (2021), p. 2000327*
[82] Gemmel et al., Phys. Rev. Applied 19, 054019 (2023)
[83] M. I. Kolobov et al., J. Opt. 19 (2017) 054003

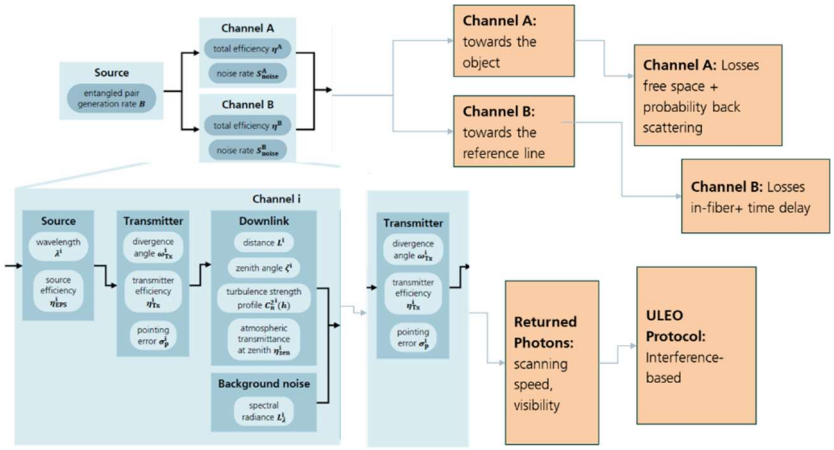

Figure 4.5.3. Flow diagram of the code for interference based imaging system

4.5.3 Correlation based-algorithm

In this approach the evaluation of the correlation is done in the same way as for QKD protocol. Considering a timing system which introduce a jitter and an additional loss in efficiency due to the features expected on the receiver detection module. Here, we estimate all the counts coming from the SPDC process as

$$S^i_{true} = \eta^i_{eps} G \qquad (10)$$

Where η^i_{eps} represents the intrinsic heralding of the EPS means the efficiency of production of the SPDC process on the Crystal itself. This true counts in a timing system are mixing with other sources of photon counts like dark counts (S^i_{dark}) and the Spectral irradiance (S^i_{back}) from light source as the Sun. This mixture can be counted by

$$S^i_{det} = S^i_{true} + S^i_{back} + S^i_{dark} \qquad (11)$$

with these single counts the coincidences are defined as

$$C_{\text{true}} = \eta^{\text{A}} \eta^{\text{B}} G\,. \quad \ldots.(12)$$

For the true coincidences and,

$$C_{\text{acc}} = \frac{\left(1 - e^{-S^{\text{A}}_{\text{det}} \tau}\right)\left(1 - e^{-S^{\text{B}}_{\text{det}} \tau}\right)}{\tau}, \qquad (13)$$

For the accidental coincidences were the τ is the coincidence window for the correlation measurement.

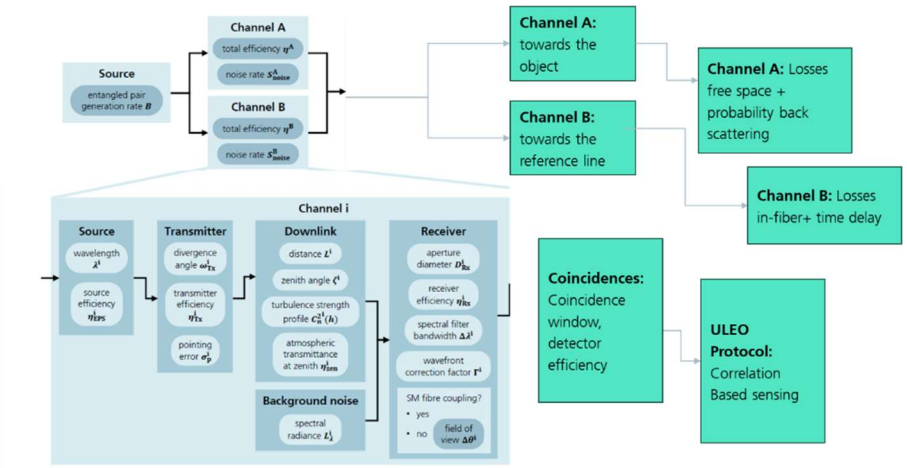

Figure 4.5.4. Flow diagram of the code for correlation based imaging system. Left diagram is the heritage from the QKD code. Right side are the modification required to have a functional code to evaluate the CAR on the backscatter photons.

Finally, the ratio between these coincidences is the coincidence to accidental ratio (**CAR**) the we use to evaluate the performance of the system in the correlation-based model.

4.5.4 General Comparison with the classical LIDAR Model

A quantum imaging system for Earth observation would offer several key advantages over a classical LiDAR.

- **Improved Signal-to-Noise Ratio (SNR):** Classical LiDAR struggles with noise from ambient light, like sunlight, which can overwhelm the weak return signal. A quantum system using **entangled photon pairs** can filter out this noise. The system sends out one photon of an entangled pair and keeps the other as a reference. By measuring the correlation between the returned photon and its "idler" partner, it can effectively ignore non-correlated background noise. This allows for superior performance in high-noise environments, such as during the day, which is a major limitation for classical systems.
- **Enhanced Sensitivity:** Quantum systems can operate with extremely low power levels, even down to a single photon. This **photon efficiency** means less power is needed to illuminate a target, which is critical for satellite-based systems where power is a precious resource. Additionally, quantum sensing for EO can leverage on "two-color" schemes offered by frequency correlations of photon-pairs, with the possibility to replace IR cameras and detectors with VIS ones; regarding this aspect, interference-based approaches offer a further advantage compared to correlation-based ones: while the

former would just need a VIS camera for NIR and MIR sensing, the latter would additionally need an IR point detector, and their operation would be limited to the NIR.

To further elaborate on the comparison, we consider the classical description of a LiDAR equation as [84]:

$$P(R) = \frac{C}{R^2}\left[(\beta_{aer}(R) + \beta_{mol}(R))\,T^2(R)\right] + \frac{C}{H^2}\frac{A_s}{\pi}\rho\cos(\theta)T^2(H) \quad (14)$$

Where **P(R)**: This is the received power as a function of range R. **R**: is the range from the lidar system to the scattering volume in the atmosphere. **H**: is the altitude of the lidar system above the ground. **β_{aer}(R)** and **β_{mol}(R)**: These are the volume backscatter coefficients for aerosols and molecules at range R, respectively. They represent the fraction of light scattered backward per unit distance by these atmospheric constituents. **T(R)**: This is the atmospheric transmission factor to range R, which accounts for the attenuation of the laser beam as it travels through the atmosphere. It is expressed as $T(R)=\exp(-\int_0^R \alpha(r')dr')$, where $\alpha(r')$ is the total extinction coefficient (from both aerosols and molecules) at range r′. The transmission term appears as $T^2(R)$ to account for the two-way path of the light (from the lidar to the scattering volume and back). **A_s**: is the area of the laser footprint on the surface. **ρ**: This is the surface albedo, which is the fraction of the incident light that is diffusely reflected by the surface. It is a dimensionless quantity that ranges from 0 for a perfectly black surface to 1 for a perfectly white surface.**θ**: This is the angle between the laser beam and the normal to the surface. The cos(θ) term accounts for the projection of the surface area onto the plane perpendicular to the laser beam, and **T^2(H)**: This represents the two-way atmospheric transmission from the lidar to the ground.

C: This is the lidar system constant, which encapsulates the characteristics of the lidar instrument itself, including the transmitted laser power, the area of the receiver telescope, and the overall system efficiency. It is typically determined through calibration as

$$C = P_0 \cdot \frac{c\tau}{2} \cdot A \cdot \eta \quad (15)$$

Where **P_0** is the transmitted power in watts, the $c\tau/2$ determines the range resolution of the LiDAR, **A** is the receiving area of the Telescope, and η is the overall system Efficiency which commonly count for the Optical Transmission (η_{opt}) The efficiency of the receiving optics (mirrors, lenses, filters). , the Detector Quantum Efficiency (η_{det}), and the Overlap Factor (O(R)): While sometimes treated separately, the overlap between the transmitted laser beam and the telescope's field of view can be considered part of this constant for ranges where it is fully overlapped (O(R)=1).

[84] *Kovalev, V. A., & Eichinger, W. E. (2004). Elastic Lidar: Theory, Practice, and Analysis Methods. John Wiley & Sons*

Now considering the eq. 7, we observe that both of the expressions take count of the loses due to the distance of the sensed object. The classical approach use the range R or H to approach the gain of the system and the Free space lose by A_r/R^2 or A_r/H^2 instead the eq. 7 we use the description from the laser communication as $G_{Tx}G_{Rx}L_{FS}{\sim}0.55\frac{D_{tx}D_{Rx}}{\lambda^2 R^2}$. In both of the models the atmospheric loses are included. However, in the classical case it is limited to the interaction range while in the eq 7, we consider the full atmosphere be crossed by the photon path.

4.5.5 Simulation Results for Return signal

For each simulation we will need to provide the parameters for each scenario.

The selected wavelengths to this initial exploration will be motivated for the technological maturity of our technique at 1550nm (c-band, already tested in lab), and 3000 nm (fundamental study phase by engineering the Non-linear crystal). Besides the technical difference in the methodological approach these ranges are of interest on Missions as MERLIN[85]. Non restricted only to LIDAR practices and extending to remote sensing, we can consider Table 4.5.2.

Table 4.5.2 Classical applications selected wavelengths (1550 nm and 3000nm)

Wavelength	**Spectral region**	**Main applications**	**Examples**
1550 nm (1.55 µm)	SWIR reflectance	- Vegetation/soil moisture and plant stress indices (e.g., NDMI) - Burned area/severity (with NIR or 2.1 µm) - Water/snow/ice discrimination; snow grain size - Water body delineation (water is dark in SWIR) - Eye-safe LiDAR (topographic, Doppler wind) - Gas remote sensing near this band (CO2 ~1.57 µm, CH4 ~1.65 µm)	- Atmospheric "window" near 1.6 µm; good for surface imaging - Example bands: Landsat 8 SWIR1 (1.57–1.65 µm), Sentinel-2 B11 (1610 nm)[86][87][88][89][90][91]
3000 nm (3 µm)	Edge of MWIR; strong H2O absorption	- Thermal hotspot detection in 3–5 µm window (fires, flares, volcanoes; esp. ~3.7–4.0 µm) - Night-time thermal imaging of warm targets - Hydrocarbon gas imaging (CH4) via strong absorption near ~3.3 µm (OGI) - Hydration/OH mapping (2.7–3.1 µm) for minerals/planetary surfaces	- Strong atmospheric H2O absorption at 2.7–3.1 µm [92]limits Earth reflectance use; thermal window opens near 3.9 µm

[85] *Ehret, G.; et al. MERLIN: A French-German Space Lidar Mission Dedicated to Atmospheric Methane. Remote Sens. 2017, 9, 1052. https://doi.org/10.3390/rs9101052.*
[86] ESA, Sentinel-2 User Handbook (MSI bands incl. B11):
[87] USGS, NDMI index (NIR–SWIR moisture):
[88] Xu (2006) MNDWI for water (uses green–SWIR): Int. J. Remote Sens. 27(14):3025–3033
[89] Key & Benson (2006) NBR burn severity: USDA RMRS-GTR-164-CD
[90] OCO-2 CO2 in 1.61 µm band (passive): Crisp et al. (2017), Remote Sens. Environ. 209: 689–701
[91] TROPOMI CH4 at 1.65 µm (passive): Hu et al. (2018), Atmos. Meas. Tech. 11: 6439–6450
[92] Ice/snow optical absorption in SWIR/MWIR: Warren & Brandt (2008), JGR 113:D14220

Wavelength	Spectral region	Main applications	Examples
			- [93]Examples: VIIRS 3.74 µm[9495], MODIS 3.96 µm (hotspots); 3 µm hydration widely used in planetary spectroscopy[96]

As shown in the table in the classical regime these wavelengths has been used for different sensing scenarios. However, It is clear that these classical application will not be match completely the quantum imaging techniques and are mention just as explorative motivation.

By employing our code we evaluate an quantum imaging setup equipped with an EPS source producing signal and idler at different wavelengths as follow:

a) Signal (traveling photons path): 1550 nm for detecting; idler (in satellite photons): 810 nm
b) Signal : 3000 nm; idler : 810 nm

These evaluations are calculated for correlation-based and interference-based approaches. For correlation-based scenario, for wavelengths >2400nm, InGaAs SPADs do not work anymore; MIR SNSPDs are being investigated from a fundamental perspective[9798], but no detector is currently commercially available. No other MIR single-photon detector are at present available. Hence by this reason we will not calculate the CAR values for the 3000nm wavelength.

For an initial evaluation, it is interesting to explore different scenarios in which the back scattering probabilities are orders of magnitudes different. For that reason, we selected *aerosols*, clouds and *Earth surface* as categories for sampling and evaluate the techniques here described with the input parameters in Table 4.5.3. The backscattering probability has been calculated as described in the 4.5.1 section for aerosols, and the classical regime is calculated by using the expression in Eq.14. For these simulations, an emitted photon flux of **10^{20} photons/s** is considered when evaluating the high gain regime for the quantum approach.

Tables 4.5.4 and 4.5.5 show the calculated returned photon flux, visibility (when considering an interference-based scheme), and CAR (when considering a correlation-based scheme), for both low and high gain regimes for different backscattering species. For comparison, the returned photon flux for a typical classical (see eq. 14) approach is also given. The difference between the

[93] MODIS active fire algorithm (3.9 µm): Giglio et al. (2016), Remote Sens. Environ. 178:31–41
[94] VIIRS 375 m fire product (3.74 µm): Schroeder et al. (2014), Remote Sens. Environ. 143:85–96
[95] Methane OGI near 3.3 µm: Ravikumar et al. (2019), Elem. Sci. Anth. 7:3
[96] Lunar/planetary 3 µm hydration: Pieters et al. (2009), Science 326:568–572; Sunshine et al. (2009), Science 326:565–568

[98] V. B. Verma, APL Photon. 6, 056101 (2021); doi: 10.1063/5.0048049

returned photon flux when considering a classical or a quantum approach mainly relies on the overall efficiency of the whole system consider per model. For the classical system we consider a system efficiency of 50% considering the detection efficiency of the receiver and the probability that a scatter photon is collected by the receiver as described in eq.14. In the so called quantum case we calculated the loss from the photon output up to its return to the receiver as shown in eq. 6 and 7. However, if we were used the same model to evaluated the loss on the down-uplink of the photon path, the usable photons will depends mainly on the detection efficiency of the receiver at the wavelength of evaluation.

These parameters can be used to discuss the feasibility of both quantum approaches in terms of a more commonly used parameter for the classical regime, For a correlation-based configuration, the CAR can be considered equivalent to the SNR since the coincidences are basically the signal to be measured and the accidentals are the noise level. On the contrary, for an interference-based scheme, the visibility cannot be directly considered as a measure of SNR but rather as a measure of system accuracy: the higher the visibility, the smaller the transmission and phase changes that the system is able to detect. To get an idea of the SNR for interference-based schemes, the signal can be understood as the returned signal flux while the noise can be taken as the background photon flux from the solar irradiance given in Table 4.5.6.

The visibility values are calculated from Eq. 8 and 9 considering that the signal and pump beams experience no losses. Therefore, the visibility values calculated have to be considered as an estimation of its lower limit because it corresponds to the case of completely unbalanced arms. Balancing the arms, or in other words, counterintuitively introducing losses in the pump and detected beam channels would improve the distinguishability between modes and improve the visibility[99]. Further improvement could be achieved in the high gain regime by optimizing the gain of the source[100].

Table 4.5.3 Input Parameters required for the calculations

Parameter	**values**
Wavelength traveler photon [m]	1.55e-06
Wavelength satellite photon[m]	8.1e-07
EPS_intrinsic_pair_generation_rate [pair/s]	20000000.0
EPS_intrinsic_heralding_efficiency_traveler photon	0.8
'EPS_intrinsic_heralding_efficiency_Bob'	0.8
atmospheric_transmittance_at_zenith'	0.92 (1550 nm), 0.26 (3000nm)
'background_spectral_radiance'	1
'zenith_angle_transmitter'[rad]	0.0

[99] Gemmel et al., Phys. Rev. Applied 19, 054019 (2023)
[100] M. I. Kolobov et al., J. Opt. 19 (2017) 054003

'zenith_angle_Receiver'[rad]	0.0
'satellite_orbit altitude [m]	540000.0
'transmitter_aperture_diameter [m]'	0.5
'transmitter_pointing_jitter [s]	1e-06
transmitter_optics_transmittance	0.75
'receiver_aperture_diameter'[m]	1.5
'receiver_obscuration_diameter'[m]	0.328
'receiver_spectral_filter_bandwidth[m]'	3e-09
'receiver_optics_transmittance'	0.6
'receiver_AO_correction_level'	full
Coupling	SMF
'MMF_core_diameter'[m]	3e-05
'MMF_numerical_aperture'	0.275
'system_timing_jitter'[s]	7.1e-10
'coincidence_window'[s]	1.2e-09
'dark_count_rate_per_detector'[cps]	300.0
'detector_efficiency'	0.7
'QKD_baseline_error_rate'	0.02
'error_correction_efficiency'	1.22,
'detection_time_jitter_per_site [s]	4e-10

Table 4.5.4. Calculation result for different scenarios LG and HG for quantum imaging in an elastic Lidar backscattering configuration.

Backscatter environment	**Back scattering probability**	**Loss [1] [dB]**	**Quantum Imaging Approach**						***Classical regime[4]***
			Low Gain[2]			**High Gain[3]**			
			RP[5] [Photons/s]	**CAR[6]**	**VIS[7]**	**RP**	**CAR**	**VIS**	**RP [Photons/s][8]**
Photon Traveling at 1550 nm									
Ice Clouds	*1.36e-2*	*-34.7*	*6.63e+3*	*35.51*	*6.63e-3*	*6.64e+16*	*4.24e+7*	*1.33e-3*	6.034e+06
Water clouds	*5.98e-3*	*-38.4*	*2.92e+3*	*29.74*	*2.92e-4*	*2.92e+16*	*1.87e+7*	*5.85e-4*	2.653e+06
Urban Aerosol	4.46e-5	-59.6	21.821	0.75	2.18e-6	2.18e+14	1.39e+5	4.36e-6	1.979e+04
Fresh Snow	8.50e-1	-16.8	4.16e+5	41.82	4.16e-2	4.15e+18	2.65e+9	8.29e-2	3.771e+08
Vegetation	3.00e-1	-21.3	1.46e+5	41.59	1.46e-2	1.46e+18	9.39e+8	2.94e-2	1.331e+08
Water surface	6.00e-2	-40.5	2.93e+4	40.28	2.93e-3	2.93e+17	1.87e+8	5.86e-3	2.662e+07

Photon Traveling at 3000 nm									
Backscatter environment	Back scattering probability	Loss [1] [dB]	Quantum Imaging Approach						*Classical regime*[4]
			Low Gain[2]			**High Gain**[3]			
			RP[5] **[Photons/s]**	**CAR**[6]	**VIS**[7]	**RP**	**CAR**	**VIS**	**RP [Photons/s]**[8]
Ice Clouds	0.007014	-57.7	33.80	--	3.38e-6	3.38e+14	--	6.76e-6	8.795e+05
Water clouds	0.003094	-61.3	14.91	--	1.49e-6	1.49e+14	--	2.98e-6	3.879e+05
Urban Aerosol	2.30e-5	-82.6	0.111	--	1.11e-8	1.11e+12	--	2.22e-8	2.884e+03
Fresh Snow	8.50e-1	-36.9	4096.91	--	0.00041	4.09e+16	--	0.00082	1.172e+08
Vegetation	3.00e-1	-41.4	1445.97	--	0.00014	1.45e+16	--	0.00029	4.138e+07
Water surface	6.00e-2	-48.4	289.194	--	2.89e-5	2.89e+15	--	5.78e-5	8.275e+06

1. Loss calculated with the previous described model for only the traveling path towards the observation object.
2. ~**10^7** photons /s on the emission from Satellite [101]
3. **~10^{20}** photons /s emitted photon flux expected from a future high gain SPDC source
4. 150mJ laser at 770nm~10^{17}photons/s
5. Returned Photons to the receiver telescope on Satellite in photons/s
6. Coincidence to Accidental ratio figure of merit for coincidence correlations approach
7. Visibility of the fringe pattern with the returned entangled photons.
8. Considering that we could have a Laser of 150mJ and 5ns pulse width, 30Hz RR at 1550nm

In the previous calculation we had been used a modeling that has been heritage from the QKD dual-downlink case. In which for each link we have one emitter and one receiver adding Gain to the optical system helping to reduce the losses. However, in the particular case for EO we will have a down-uplink configuration with only one transmitter and one receiver, we modified the code to adjust it to this particular scenario where the increasing of the losses is expected as shown in the Table 4.5.5.

[101] *E. Brambila et al., Opt. Express **31**, 16107-16117 (2023)*

Table 4.5.5. Results by modifying the optical architecture for Down-uplink configuration

Backscatter environment	Back scattering probability	Loss [1] [dB]	Quantum Imaging Approach						*Classical regime*[4]
			Low Gain[2]			High Gain[3]			
			RP[5] [Photons/s]	CAR[6]	VIS[7]	RP	CAR	VIS	RP [Photons/s][8]
Photon Traveling at 1550 nm									
Ice Clouds	*1.36e-2*	*-147.5*	*3.48735583e-08*	--	*3.48735583e-15*	*348735.583*	*0.709*	*6.97471167e-15*	6.034e+06
Water clouds	*5.98e-3*	*-151.1*	*1.53833801e-08*	--	*1.53833801e-15*	*153833.801*	*0.705*	*3.07667603e-15*	2.653e+06
Urban Aerosol	4.46e-5	-172.4	1.14632183e-10	--	1.14632183e-17	1146.321	0.347	2.29264365e-17	1.979e+04
Fresh Snow	8.50e-1	-129.6	2.18337241e-06	--	2.18337241e-13	21833724.095	0.720	4.36674482e-13	3.771e+08
Vegetation	3.00e-1	-134.1	7.70602027e-07	--	7.70602027e-14	7706020.269	0.714	1.54120405e-13	1.331e+08
Water surface	6.00e-2	-141.1	1.54120405e-07	--	1.54120405e-14	1541204.053	0.711	3.08240811e-14	2.662e+07
Photon Traveling at 3000 nm									
Ice Clouds	0.007014	-154.6	6.79199 44e-09	--	6.79199 44e-16	67919.9	0.699	1.35839 888e-15	8.795e+05
Water clouds	0.003094	-158.2	2.99607 062e-09	--	2.99607 062e-16	29960.7	0.684	5.99214 123e-16	3.879e+05
Urban Aerosol	2.30e-5	-179.5	2.23161 948e-11	--	2.23161 948e-18	223.2	0.111	4.46323 896e-18	2.884e+03
Fresh Snow	8.50e-1	-133.9	8.23036 412e-07	--	8.23036 412e-14	8230364.1	0.714	1.64607 282e-13	1.172e+08
Vegetation	3.00e-1	-138.3	2.90483 44e-07	--	2.90483 44e-14	2904834.39	0.712	5.80966 879e-14	4.138e+07
Water surface	6.00e-2	-145.4	5.80966 879e-08	--	5.80966 879e-15	580966.8	0.710	1.16193 376e-14	8.275e+06

It is important to note the physical interpretation of the CAR in the high-gain regime of SPDC. As mentioned in Section 4.1, high-gain sources, compared to low-gain sources, feature non-negligible contributions from multiphoton pairs. However, current technology only permits coincidence measurements for a single pair of photons, because photon-number resolving detectors—even though recently made commercially available—still do not provide true photon-number resolution, making multiphoton coincidence measurements unfeasible. Consequently, coincidence measurements with high-gain sources are possible but exhibit lower CAR values than

their low-gain counterparts, due to the contributions from multiple photon pairs. In Table 4.5.6, the CAR column for high-gain cases was calculated without differentiating multiphoton events on the detection side. Accordingly, these values are exponentially higher than the calculated values for low-gain sources.

An additional evaluation can be made by changing the environmental noise due to the Solar radiance. Considering the correlation-based technique, we require to couple the light into a SMF to make the coincidence counting, this background could be calculated as:

$$R\_bg \approx \eta_{Rx}\ \eta_{det}\ L\lambda\ A\Omega\_eff\ \Delta\lambda \times (\lambda 0 / hc)$$

Where the $\eta_{Rx}\ \eta_{det}$ are the efficiencies for the Rceiver and the detector, $L\lambda$ is the average Solar Spectral radiance per bandwidth, $A\Omega\_eff$ is the effective collection on the SMF commonly limited by λ_0^2, $\Delta\lambda$ is the spectral bandwidth on the detection, and λ_0 the evaluation wavelength. For this evaluation, we take the the Solar Spectral radiance taking 1W/sr/m^3 for the night time (sun below the horizon) and 10^{6}W/Sr/m^3 (Direct sun at top of Atmosphere)as average values per bandwidth as shown in the following table.

Table 4.5.6. background values for two Solar Spectral irradiance scenarios in the background (night and day time)

	Solar Spectral Radiance average [W/sr/m^3]	
λ_0 [nm]	1 W/sr/m^3	1E6 W/sr/m^3
3000	0.217 cps	21299 cps
1550	0.029 cps	29988 cps

The solar irradiance can be considered as a source of noise and, in a correlation-based quantum sensor, it contributes to the accidental counts. Therefore, considering the amount of solar irradiance from Table 4.5.6 together with the calculated amount of returned photons given in Tables 4.5.4 and 4.5.5, the performance of the interference- and correlation-based quantum sensing approaches can also be analyzed in terms of SNR and the distillation capabilities demonstrated in the literature[102,103] to calculate the minimum photon flux required for each scenario considered to work. The following discussion analyses the case where 1550nm light is used as probe wavelength, but the same can be adapted to different wavelengths. From the losses presented in Table 4.5.4 and 4.5.5, the returned photon flux can be calculated (also given in the mentioned Tables). The minimum required emitted photon flux can be then calculated as the ratio between the day(night) solar irradiance and the experimental distillation limit demonstrated for interference- or correlation-based configurations.

[102] T. Gregory et al., Sci. Rep. **11**, 21841 (2021)
[103] J. Fuenzalida et al., Sci. Adv. **9**, eadg9573 (2023)

For an interference-based approach, assuming the experimental limit demonstrated experimentally in the literature where noise intensities 250 times higher than the quantum signal can be distilled[103], a minimum returned signal of 1.16E-4 photons/s would be required for night-time operation and 120 photons/s for day-time operation (where the correspondent noise fluxes for the calculation are taken from Table 4.5.6 as 0.029cps and 29988 cps for night- and day-time operation, respectively). From this we can conclude that for night time operation, the noise level could be distilled from the quantum signal for all cases analyzed in Table 4.5.4, even for a low gain scenario. Since the background noise coming from solar irradiance for day time operation is ~29988 photons/s, not all scenarios in a low gain regime would be able to distill the noise, but a high gain operation with 10^{20} emitted photons/s would ensure distillation of the quantum signal from the noise. Unfortunately, a high gain source with this amount of photon flux has not been demonstrated yet. Furthermore, from the losses calculated in Table 4.5.5, which is a more realistic approach for interference-based quantum sensing scenarios, the minimum emitted flux required for day-time operation would be in the range of 10^{15} to 10^{19} photons/s for the examples considered. For night-time operation, the emitted photon flux required lowers to a range between 10^{9} and 10^{13} photons/s.

In addition, the low visibility for both scenarios (low and high gain) would make necessary longer exposure times unless compensation techniques to improve the visibility values are used[104,105].

For a correlation-based approach, the CAR is the equivalent to the SNR since the coincidences are the measured signal while the accidentals are the noise level. In that case, a CAR down to 0.05 or in other words a returned photon flux of 1.45E-3 photons/s for night-time operation and of ~1500 photons/s for day-time operation (when considering the 0.029cps and 29988 cps, respectively, as noise photon flux given in Table 4.5.6), would allow to distill the quantum signal from noise according to the demonstrated ratio in the literature of 1:20 (SPDC signal:thermal noise)[102]. CAR values above the limit are only expected for the high gain scenario considered in the Table 4.5.5. From the losses calculated in Table 4.5.5, the minimum emitted flux required for day-time operation would be in the range of 10^{16} to 10^{20} photons/s for the examples considered. For night-time operation, this requirement relaxes to a range between 10^{10} and 10^{14} photons/s.

Therefore, the state-of-the-art high gain sources[106] with emitted photon flux ~10^{12} photons/s would allow only night-time operation for selected applications in both, interference- and correlation-based configurations. Higher photon flux sources (above 10^{15} photons/s) would be required to ensure continuous operation of quantum sensors for EO.

Finally, we can estimate approximate the cross-tracking values for this technique as the footprint of the photons over the Earth surface by employing the divergence half angle

$$R_f = R_l tg(\theta)$$

[104] Gemmel et al., Phys. Rev. Applied 19, 054019 (2023)
[105] M. I. Kolobov et al., J. Opt. 19 (2017) 054003
[106] Hashimoto, K. et al., Commun Phys 7, 217 (2024). Amplified signal flux considering they have: 15ps laser pulse which translates into a 15ps SPDC pulse, repetition rate of 1kHz, signal average power of 580nW, and signal wavelength 600nm

Where Rl is the link length from satellite to Earth and θ is the half angle beam divergence given by

$$\theta = M^2 \frac{\lambda}{\pi w_0}$$

With these calculation we reach values of 1.59 km for the 1550 nm footprint and 3.09 km for the 3000nm wavelength. However the axial resolution of the technique will be limited mainly for the Delay line and the bandwidth of the SPDC beam. Currently in the lab we has been used coherence lengths with a 1.5nm filter of 0.42mm, even with a 10nm filter the coherence length is even shorter (0.15mm). Idler wavelength is 730nm with FWHM 5.2nm. For correlation case is a mix of the electronical delay line in which the coincidence window does not influence the axial resolution, but optimizes the quantum characteristic of the arrival photons to evaluate the correlations within the defined interval. For the scanning approach, the resolution will be determined by the FOV at the Earth surface. For wide-field imaging approach exploiting momentum correlations of the generated photon pair, resolution will be dependent on the SPDC wavelengths, the imaging system (focal length of the emitter optics, and magnification system), the pump waist at the crystal, and the crystal length.

$$\Delta_{\mathrm{V_{MC}}} = \frac{f_{\mathrm{u}}\lambda_{\mathrm{u}}}{\sqrt{2}\pi\omega_{\mathrm{p}}} \sqrt{\frac{2\pi{\omega_{\mathrm{p}}}^2(\lambda_{\mathrm{d}}+\lambda_{\mathrm{u}})\left[2\pi{\omega_{\mathrm{p}}}^2(\lambda_{\mathrm{d}}+\lambda_{\mathrm{u}})+L{\lambda_{\mathrm{u}}}^2\right]}{\left[2\pi{\omega_{\mathrm{p}}}^2(\lambda_{\mathrm{d}}+\lambda_{\mathrm{u}})-\lambda_{\mathrm{d}}\lambda_{\mathrm{u}}L\right]^2}} M_{\mathrm{u}} \quad [107]$$

Under certain parameter regimes, the above expression can be simplified to[108]:

$$\Delta_{V,\mathrm{o}} = \frac{f_{\mathrm{u}}\lambda_{\mathrm{u}}}{\sqrt{2}\pi\omega_{\mathrm{p}}} M_{\mathrm{u}}$$

Considering the variable involve in each of the techniques we will be able to estimate properly the values for the expected axial resolution.

4.6 WP4100 – WP4200: Risk mitigation strategies

The initial evaluation of the challenges and risks of bringing different quantum sensing approaches to a satellite configuration for Earth observation applications (presented in Sec. 4.2) has been reviewed and updated with possible mitigation strategies as a result of the work performed on the framework of the ULEO project. A description on the risks and mitigation strategies can be found in the table "RiskMitigation.xlsx" attached in the documentation package for better readability.

The main conclusion from the returned signal analysis presented in Sec. 4.5 is that sources with photon fluxes above 10^{15} photons/s are required to ensure continuous operation of a quantum

[107] Publication in preparation
[108] J. Fuenzalida et al., Resolution of quantum imaging with undetected photons, Quantum 6, 646 (2022)

sensor for EO. Current state-of-the-art high gain sources[109] with emitted photon flux ~10^{12} photons/s would only allow night-time operation for selected applications in both, interference- and correlation-based configurations.

Assuming a source emitting photon flux above 10^{15} photons/s can be developed with currently available technology, main conclusions from this risk and mitigation strategies study are:

a) Correlation-based approaches seem feasible for Earth observation applications but with a limited quantum advantage.

The main limitation for correlation-based approaches comes from the fact that NIR detection is currently only feasible until 2400nm, and there are no SPDs available for longer wavelengths. Moreover, the overall efficiency decays with the efficiency of both, visible and IR detectors, while for interferometric approaches only the visible detector would introduce a loss.

Although the results from the analysis performed in the ULEO project indicate that correlation-based approaches could be feasible for Earth observation applications when operated in a high gain regime, further studies are necessary to completely evaluate their feasibility for EO applications. Our results in Section 4.5 only consider losses in terms of backscattering probability; but influences coming from any optical component after back-reflected light gets collected by the satellite telescope are not considered. In a hain gain scenario, coincidence counting would still be possible, however with reduced CAR due to the non-negligible multi-pair contribution, thus potentially cancelling any quantum advantage acquired through VIS camera operation. Nevertheless, a correlation-based approach could also benefit from a quantum advantage regime in terms of SNR improvement in the low-gain regime (photon-pairs), whereas the extension to the high-gain is not yet established and could cancel such advantage.

b) Interferometric-based approaches seem feasible for Earth observation applications.

When operated in a high gain regime, the technique would ensure performance for all analysed scenarios. Moreover, the results from the initial experimental study performed indicate that the strength of the position correlations between down-converted photons (directly related to the image resolution) would be robust to atmosphere turbulences. Nevertheless, further studies are necessary to completely evaluate the feasibility of interference-based sensing techniques for EO applications.

Some of the necessary follow-on studies related to interference-based approaches can be conducted internally by IOF, while others would require the involvement of external partners with specific expertise. We focus on the interference-based approach because it would offer a broader

[109] Hashimoto, K. et al., Commun Phys 7, 217 (2024). Amplified signal flux considering they have: 15ps laser pulse which translates into a 15ps SPDC pulse, repetition rate of 1kHz, signal average power of 580nW, and signal wavelength 600nm

range of applications compared to a correlation-based configuration, as the latter is limited by the lack of commercial MIR single-photon detectors. The key challenges that must be addressed to enable a thorough evaluation of the feasibility of interferometric-based approaches are, in order of criticality:

1. Basic research to increase high gain photon flux. The high gain source demonstrated in the literature with 10^{12} photons/s used a pump pulsed laser with 15ps pulse width, 1kHz repetition rate, and peak energy up to 0.9mJ. Higher pulse powers are available in commercial lasers, i.e. Yb ultrafast lasers, where pulse energies up to 20 mJ can be delivered (e.g. by Active Fiber Systems GmbH in Jena https://www.afs-jena.de/products/ytterbium-lasers-high-power/). The required study should demonstrate that the current state of technology allows to develop high-gain sources with fluxes high enough to guarantee both day and night operation. Importantly, nonlinear crystal damage threshold should be carefully evaluated; alternatively strategies making use of high power lasers together with seeding techniques can be envisioned to reach the same goal.
2. More detailed evaluation considering exact loss parameters after collection of the returned photons with the telescope. That would allow to fairly compare the performance of the systems between low- and high-gain regimes, and classical systems. This is necessary to conclude on feasible operation regimes.
3. Evaluation of the quantum advantage for a high gain scenario in terms of overall payload. Collaboration with external expertise would be needed to quantify the minimum payload of the overall system for the design of an engineering qualification model. Nevertheless, an initial estimation comparing an hypothetical classical sensing system with its quantum counterpart is presented in the table below (Table 4.6.1). For the classical system, the IPDA instrument from the MERLIN mission is accounted as the laser system, and a commercial MCT detector as the detection system. The selection of the IPDA instrument is based on the wavelengths used for illumination, which are beyond the detection range of most Si-based detectors. The mission uses InGaAs Avalanche Photodiodes for CH_4 detection. For these measurements, there is another atmospheric window around 2300nm but the efficiency of the detectors is lower. Motivated by this example, we envision an hypothetical mission that would benefit from illumination at longer wavelengths, for example in the 10 µm range, which would require MCT detectors. For the quantum counterpart, we take the laser system used in the literature to achieve high gain operation of a quantum sensing system[110] and an example of a photodetector similar than the one they might have used[111].

[110] Hashimoto, K. et al., Commun Phys **7**, 217 (2024)
[111] https://www.thorlabs.com/newgrouppage9.cfm?objectgroup_id=6686&_gl=1*1i61kxb*_up*MQ..*_gs*MQ..&gclid=EAIaIQobChMI0_7F3tKFkAMVlPp5BB3REBPmEAAYASAAEgLQgPD_BwE

Table 4.6.1 Comparison between a classical sensing mission payload (combination of the IPDA instrument and an hypothetical MCT detector) and its quantum counterpart

	Classical sensing	**Quantum sensing [2]**
Laser volume	820x830x1010mm^3 [1] (*)	500x1031x249mm^3
Laser power supply		365x395x290mm^3
Detector volume	356x87x67mm^3 [3]	75x56x28mm^3 [4]
Detector cooling	Yes, liquid nitrogen	Yes, air cooling

[1] https://www.eoportal.org/satellite-missions/merlin#instrument
[2] Hashimoto, K. et al., Commun Phys **7**, 217 (2024)
[3] https://irassociates.com/index.php?page=ln2-cooled
[4] https://www.thorlabs.com/newgrouppage9.cfm?objectgroup_id=6686&_gl=1*1i61kxb*_up*MQ..*_gs*MQ..&gclid=EAIaIQobChMI0_7F3tKFkAMVlPp5BB3REBPmEAAYASAAEgLQgPD_BwE
(*) IPDA instrument payload volume

For classical sensing, the payload of the entire IPDA instrument is considered, as no specific information on the laser subsystem payload could be identified in the literature. For quantum sensing, by contrast, the comparison is based on the laser head and power supply reported in the literature for operation in the high-gain regime. As a result, this does not constitute a strict one-to-one comparison: in the classical case, the full instrument payload—including additional subsystems beyond the laser—is taken into account, whereas in the quantum case, only the laser subsystem is considered. It should also be noted that the comparison is not entirely equitable for quantum sensing either, since the reported laser source has not yet been optimized for space applications.

A narrow linewidth laser would be necessary to ensure operation for EO applications; external expertise on narrow linewidth lasers for space applications would be required for a more thorough comparison, as custom systems beyond off-the-shelf commercial ones might be needed.

4. An extension of the turbulence resilience studies of the undetected light protocol should be performed for the high-gain case. In parallel, intermediate tests could be performed by taking advantage of the IOF free-space link (~1.4 km); to such end, collaborations with scientific groups active in quantum sensing with squeezed light/high-gain sources might bring an added value.

5. Design and study on the most suitable delay line approach. Three main approaches have been identified: (1) free-space Herriot cell with custom high-reflectivity coatings (R~0.99999 would lead to 35 dB losses for 800 km delays). To this end, Fraunhofer IOF possesses internal knowledge within the "Optomechatronical Components and

Systems" and "Functional surfaces and coatings" departments. (2) fiber-based delay line, in conjunction with amplifiers for signal and pump fields, similarly to what has implemented for quantum communication purposes[112]. (3) satellite constellation approach to minimize optical losses. This approach would specifically require external collaborations.

6. Fundamental research on the physics of induced coherence to identify potential interference-free approaches to implement two-color schemes; this would avoid the need of a delay line. As an example, MIR spectroscopy with NIR detection has been experimentally demonstrated in photonic integrated structures, without the need of a full nonlinear interferometer[113]; the identification of similar approaches and their adaption to EO scenarios would require further fundamental research.
7. Quantification of the effect of atmospheric losses in a high gain scenario to verify the model developed in ULEO and identify optimal mitigation schemes. IOF possesses expertise within the "Photonic Quantum Systems" department on high gain sources for quantum computing; for quantum sensing purposes, external collaborations might be considered.
8. Experimental evaluation of the system in real environment (free-space link). IOF has the expertise and infrastructure for this evaluation.
9. Assess the necessary optics engineering mechanism to ensure the overlap and indistinguishability between the returned signal and the backward generated signal in the satellite. Here two main mitigation strategies might be necessary: (1) wavefront shaping techniques and adaptive optics; to this end IOF possesses expertise in adaptive optics for satellite-based quantum communication within the "Laser and Fiber technology" department. (2) polarization compensation; the "Photonic Quantum Systems" department already offers such service for free-space links and physical optical fiber infrastructures in quantum communication applications.
10. Assess specific orbit requirements based on targeted EO application to optimize the data acquisition process. External collaborations/expertise is needed to this end.
11. Identification of the optimal distillation algorithm, to mitigate the effect of losses and other detrimental effects, while improving the SNR. Two different approaches are feasible: (1) based on the interferometric modulation of the recorded signal[114] or (2) based on a hybrid undetected light – classical off-axis holography approach[115]. For both approaches, further application oriented studies are needed to identify limits and boundary conditions to noise mitigation, depending on specific use-cases. Additionally,

[112] M. Cizek et al., Coherent fibre link for synchronization of delocalized atomic clocks, Opt. Express 30, 5450-5464 (2022).
[113] M. Ravaro, et al., Nonlinear measurement of mid-infrared absorption in waveguides, Appl. Phys. Lett. 14, 92 (15): 151111 (2008).
[114] Jorge Fuenzalida et al., Experimental quantum imaging distillation with undetected light,.Sci. Adv. 9, eadg9573 (2023).
[115] J. R. León-Torres, et al., Off-axis holographic imaging with undetected light, Opt. Express 32, 35449-35461 (2024).

focused studies are needed to assess whether these distillation techniques enable noise resilience only, or can be adapted to other detrimental effects. Exploration on different acquisition methods or image reconstruction algorithms to apply in conjunction with distillation techniques might be relevant as well.

12. Different types of nonlinear interferometers might be considered to maximize the device stability. A high-level stability study and misalignment test was performed in IOF[116] and constitutes a starting point of such investigations; further steps should include resilience tests to vibrations for different configurations, test the nonlinear interferometer for temperature stability in a wide temperature range, perform piston tests.

Despite the number of identified challenges to develop an active interferometric quantum sensor as explained, the QIUL-derived protocol we propose could also find use as "stepping stone" system for on-satellite sensing purposes. This would significantly reduce the number of challenges to face: namely: challenges 1, and 3-9 would not apply as they are directly connected to long distance sensing. Possible applications of an on-satellite quantum sensor based on QIUL include any scenario related to gas sensing of species possessing a signature in the fingerprint region of the MIR spectrum; examples include in-platform contamination and outgassing monitoring of CO_2, CH_4, NH_3 species. A quantum sensor as proposed would be able to detect the MIR fingerprint of such gases using highly efficient VIS detectors, as already demonstrated in a proof-of-principle experiment[117]. In principle photon-pair sources working in the MIR have been demonstrated to work up to 14 µm[118], highlighting the possibility to tune the emission wavelength of the idler photon to match application needs in the fingerprint region. Similarly, the proposed quantum sensor could be applied to hydrazine derivatives sensing for leak detection; for this application, sensing in the MIR with VIS detection becomes particularly attractive, as the IR hydrazine absorption lines can be broad, and much weaker than e.g. ammonia lines[119]. Finally, the proposed QIUL quantum sensor could also be readapted for a use-case beyond EO, in satellite quantum communication. Quantum state tomography of undetected photons has been shown as a powerful tool to reconstruct the quantum state of an unknown photon without directly measuring it, i.e. without entanglement perturbation[120]; this feature can find application to establish an in-platform monitoring and diagnostic sensor to supervise the correct functioning of an entangled photon source without disturbing its operation in a quantum communication protocol, or perturbing its entangled state with direct measurements.

4.7 WP4300: Possible mission concept design

[116] M. Gilaberte Basset, et al., Video-Rate Imaging with Undetected Photons, Laser & Photonics Reviews 15, 2000327 (2021).
[117] A: V. Paterova et al., ACS Photonics 9 (6), 2151-2159 (2022).
[118] M. Kumar et al., Appl. Phys. Lett. 119 (24): 244001 (2021).
[119] S. Plunkett et al., Spectrochimica Acta Part A: Molecular and Biomolecular Spectroscopy 58, 11, 2505-2517 (2002).
[120] J. Fuenzalida et al., Phys. Rev. A 109, 022413 (2024).

Based on the literature overview together with the numerical analysis and experimental results performed along the ULEO project, we conclude that once a higher photon flux source is available (>10^{15} photons/s, compared to ~10^{12} demonstrated in the literature), the more feasible quantum sensing approaches to EO scenarios are spectroscopy and wide-field imaging in an interference-based sensing configuration.

For spectroscopy applications, the quantum mission we envision is an active spectroscopy instrument, instead of passive MIR spectroscopy missions that currently exist. This would require a change from classical passive detectors to an active approach. The idea behind is that for spectroscopy one measures the spectral bands that are absorbed by the sample and, therefore, not detected. Still, one would need to assess if the current measurements are compatible with an active approach. Nevertheless, there are two configurations of this active approach that could be analysed. One would rely on sending a broadband spectra to probe the sample, e.g. atmosphere, clouds, or aerosols, and analyse the returned spectra to find out the absorbed wavelengths[121,122]. Another configuration would rely on sending a narrowband probe spectra that is scanned to cover the whole spectra of interest[123]. Sending a narrowband spectra would have the advantage of higher photon flux per band, and therefore providing better SNR, than the broadband scenario. The drawback would be the lower analysis speed since the complete composition information would be only available after the several measurements instead of the "one-shot" scenario from a broadband probe spectra. Spectroscopy could be a specially interesting approach for measuring the presence of a specific component(s) with low-noise silicon-based detectors even when the information of the sample is in the IR, for example.

The correlation-based approach is not considered because it would require two fundamental aspects to be addressed before it can offer an advantage with respect to classical approaches. The main one is the need for the development of MIR SPDs. Currently, NIR detection is feasible until 2400nm but there are no SPDs available for longer wavelengths. The other aspect to be addressed is the development of theory and extension of a correlation protocol for a high gain scenario, the development of a quantum sensing concept based on photon number correlations in presence of losses, and would require intrinsic photon-number resolved detection (currently under development).

Among sensing modalities, the quantum scanning scenario is also initially discarded because the scanning mechanism would require further studies on galvo-galvo scanning mechanisms or resonant scanner components for its implementation. Although both approaches have already been implemented in a lab environment, external expertise would be required to adapt the design for operation from a satellite.

A possible mission concept design is depicted in the block diagram in Fig. 4.7.1. This concept relies on a two satellite constellation in order to implement a delay line that is long enough to enable

[121] C. Lindner et al., Accurate, high-resolution dispersive Fourier-transform spectroscopy with undetected photons, Opt. Contin. **1**, 2 (2022).
[122] https://arxiv.org/pdf/2507.07861
[123] S. Kyung Lee et al., Molecular rovibrational spectroscopy with undetected photons via single-photon interferometry, Phys. Rev. Applied **14**, 014045 (2020)

the quantum sensing approach. This solution is inspired by current missions that use a constellation of satellites, and the idea would be add a quantum sensor for EO to missions that would plan to make use of more than one satellite.

Nevertheless, the complexity added by the delay line should be carefully evaluated to determine whether the benefits of reduced system complexity and payload, achieved through the replacement of IR detectors with silicon technology, justify the implementation of quantum sensing for EO missions.

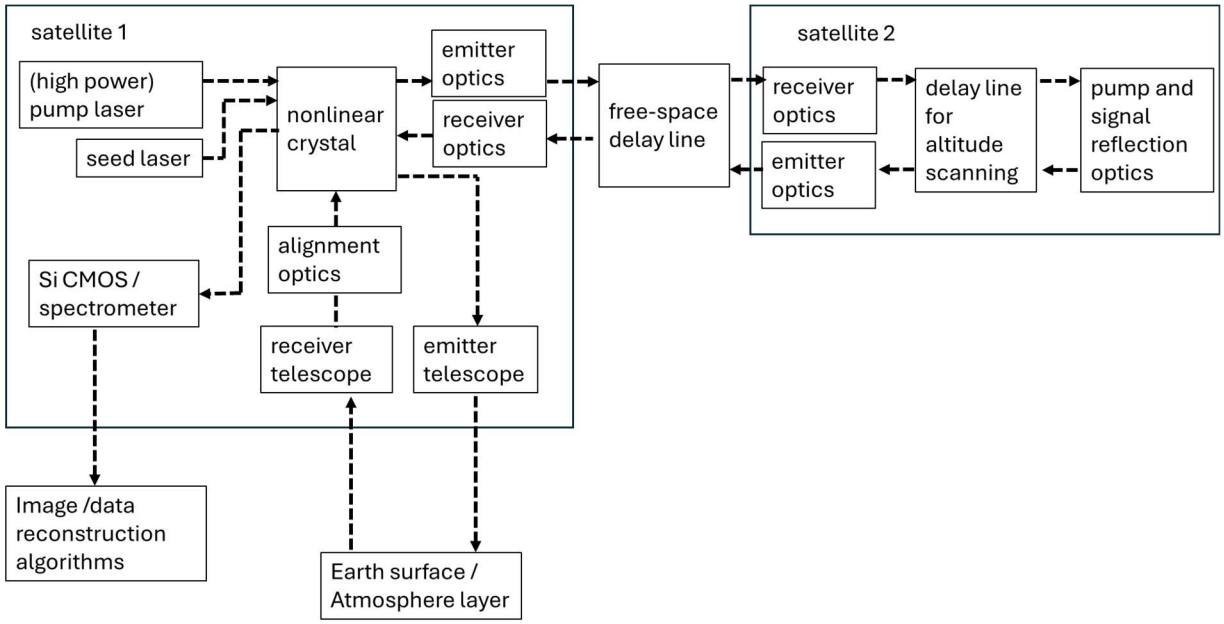

Figure 4.7.1Block diagram of a possible quantum sensing mission design

The need for operation in a high gain regime in order to have enough returned signal flux imposes the requirement to have either a high power pump laser or to use a seed laser together with a pump laser. The free-space delay line implemented between satellites it is the preferred options since it minimizes the losses.

5 FEASIBILITY SUMMARY AND OUTLOOK (WP4400)

As concluded in Section 4.6, the most viable current approach to exploit the benefits of quantum sensing for Earth observation is an interference-based configuration. Although further studies are necessary to fully demonstrate the feasibility of this technique with the current state-of-the-art, key technologies that in principle would allow this technique to be feasible for EO applications already exist. Based on the study performed in the framework of ULEO, the following roadmap is suggested.

After the ULEO project study and evaluation, the current technology readiness level (TRL) of Earth observation quantum sensing (EOQS) systems is on TRL2, and partially TRL3. In this frame, a TRL breakdown per subsystem can help to improve the clarity of this document. Components as the

pump laser, the nonlinear crystal and the sCMOS camera are themselves commercially available, and are or will be employed in space missions, for example Micius for the nonlinear crystal/source[124] and the Comet Interceptor Mission for the sCMOS sensor[125]. Assuming in a hypothetical future ULEO mission, similar components could be employed. Given the different specificity of the mission, the TRL build-up would need to start from TRL5 in the best case scenario, however at a current stage no fundamental limitations preventing the subsystems to reach TRL9 can be foreseen. The photon-pair source here employed is TRL3, however in a different project IOF has demonstrated a photon-pair source with EQM classification[126]; more critical here is the delay line, which at its current status does not reach TRL2 yet. We believe that in three years, the TRL of the overall system could be raised to TRL 4. At this stage, the feasibility of low- and high-gain regimes would be addressed with a complete analysis of the exact loss parameters after collection of the returned photons with the telescope. In any case, the focus would be to build a lab prototype in the high gain regime since this would allow for better SNRs with the trade-off of additional payload, and to quantify in detail the effects of atmosphere turbulence and losses for these sources. To quantify that, a long-distance measurement configuration in a lab environment would be set in order to initially evaluate the different engineering challenges, e.g. the delay line, or the optics necessary for a long-distance scenario. In parallel, more fundamental studies could be performed to evaluate further strategies to maybe avoid the need of a delay line, to optimize the data acquisition method, or the distillation algorithm.

After a successful demonstration of a EOQS system on TRL 4, we believe that four years would be necessary to miniaturize the system and verify it in a relevant environment (outside of the lab). The relevant environment is envision to be the free-space link that connects the IOF building with the Jena Stadtwerke building (1.5 km away).

[124] C. Y. Lu et al., Rev. Mod. Phys. 94, 035001 (2022).
[125] T. Behnke et al., Design and characterization of the sCMOS detector for the comet interceptor camera International Conference on Space Optics — ICSO 2024.
[126] ESA Space-EPS project (Photonic Transceiver for Secure Space Communications: New Space Suitable Entangled Photon Source), Call: ARTES 5.2 Call AO/1-6000/ 09/NL/US, rev. 7.

Table 5.1 Quantum Sensing techniques for earth observation roadmap

QUANTUM SENSING TECHNIQUES FOR EARTH OBSERVATION (EOQS) ROADMAP								
2024	**2025**	**2026**	**2027**	**2028**	**2029**	**2030**	**2031**	**2032**
Initial assement (ULEO)		**EOQS to TRL4**			**EOQS to TRL5-6**			
		- Complete evaluation of low gain regime for EOQS systems - Demonstrate high gain photon fluxes above 10^{15} photons/s - Evaluation of the quantum advantage for a high gain scenario in terms of overall payload - Extension of the turbulence resilience studies of the undetected light protocol - Design and study on the most suitable delay line approach - Study on the required speed and range of the delay line - Fundamental research on schemes that might avoid the need of a delay line - Quantification of the effect of atmospheric losses in a high gain scenario to verify the model developed in ULEO and identify optimal mitigation schemes - Engineering of the required overlap optics mechanism to ensure interference-based schemes operation - Identification of the optimal distillation algorithm - Evaluation of different types of nonlinear interferometers to maximize the device stability			- Assess specific orbit requirements based on targeted EO application to optimize the data acquisition process - Experimental evaluation of the system in real environment (free-space link) - Engineering design for miniaturization, robustness and stability - Environmental tests (e.g. vibration, shock, radiation, temperature)		

6 PURCHASES ITEM LIST (ANNEX)

Component	Reference	Description	Company	Price
Motorized rotary stage and stepper controller	LS-50-HR-ENC ACE-SDE	50mm motorized rotary stage with 1250 cycle encoder	Lexitek	2597$
Phaseplate design		Pseudo-Kolmogrov phase design for r0=0.5mm and r0=1.0mm	Lexitek	324$ (unit price 162$)
Phaseplate r0=0.5mm	PRP-50-FRN	50 mm diameter Near-Index-Match™ phase plate with 38mm phase OD, r0=0.5mm	Lexitek	2840$
Phaseplate r0=1.0mm	PRP-50-FRN	50 mm diameter Near-Index-Match™ phase plate with 38mm phase OD, r0=1.0mm	Lexitek	2840$

7 DELIVERABLES (ANNEX)

Documents attached in the final documentation package:

Name	Deliverable	File Name(s)	Associated file(s)
KOM	Project Bar Chart	ProjectBarChart_AfterRRM.png	
BMPR	Bi-Monthly Progress Report (reported monthly)	ULEO_RRM.pdf ULEO_TM1.pdf ULEO_TM2_WP2000.pdf ULEO_TM2_WP3000.pdf ULEO_Workshop_032025.pdf ULEO_TM3.pdf ULEO_TM4.pdf	
MTR	Mid-Term Review Report	ULEO_MTR.pdf	
MOM	Minutes of Meetings	2024-10-15_ULEO_Negotiation-Minutes_Draft_VFG FFi.pdf ULEO_MTR_03042025_MoM_sign.pdf ULEO_Requirement_Review_Meeting_2911 2024_MoM_singed.pdf	

		ULEO_Technical_Meeting_04062025_MoM_sign.pdf ULEO_Technical_Meeting_14022025_MoM_sign_JH.pdf	
WSC	Contribution to international workshop and an ESA-organised event	1578_GilaberteBasset.pptx	
FR	Final Report	FR-IOF-01.pdf	RiskMitigation.xlsx
SSP	Single Slide Presentation	Single Slide FR.pdf	

End of Document